AGU PUBLICATIONS

Radio Science

RESEARCH ARTICLE
10.1002/2014RS005513

Special Section:
URSI Symposium on Radiowave Propagation and Remote Sensing, 2013

Key Point:
- Impact of L-band scintillation on GPS receivers using real and synthetic data

Correspondence to:
F. Ghafoori,
fghafoor@ucalgary.ca

Citation:
Ghafoori, F., and S. Skone (2015), Impact of equatorial ionospheric irregularities on GNSS receivers using real and synthetic scintillation signals, *Radio Sci.*, *50*, 294–317, doi:10.1002/2014RS005513.

Received 2 MAY 2014
Accepted 12 FEB 2015
Accepted article online 18 FEB 2015
Published online 17 APR 2015

Impact of equatorial ionospheric irregularities on GNSS receivers using real and synthetic scintillation signals

F. Ghafoori[1] and S. Skone[1]

[1]Department of Geomatics Engineering, Schulich School of Engineering, University of Calgary, Calgary, Alberta, Canada

Abstract The impact of L-band equatorial ionospheric scintillation on Global Navigation Satellite Systems (GNSS) receivers is investigated in this paper using both real and synthetic scintillation data. To this end, various low-latitude data sets, recorded during the most recent solar maximum, are exploited in post-processing to develop and verify realistic simulation tools and evaluate GNSS receiver performance. A scintillation simulation model is implemented based on the phase screen formulation of Dr. Charles Rino (1979, 1982, and 2011) which allows oblique signal propagation in an anisotropic propagation medium with multiple irregularity layers (or phase screens) for multiple GNSS frequencies. The observed real scintillation parameters are used to drive GNSS signal simulations. The subsequent simulated GNSS signal time series are verified through comparison with real data for different signal tracking states including the most severe and challenging tracking scenarios. Using both real and synthetic data sets, the impact of scintillation on observation quality and receiver performance is evaluated in terms of probability of loss of phase and frequency lock, as well as the correlation of disturbed L-band signals transmitted by GNSS satellites on the same transionsopheric path.

1. Introduction

Random rapid fluctuations in the phase and intensity of received Global Navigation Satellite Systems (GNSS) signals, resulting from plasma density irregularities within the Earth's ionosphere, are referred to as ionospheric phase and intensity scintillation, respectively. Two regions on the Earth are highly prone to scintillation effects: the low-latitude region, approximately 20° north and south of the geomagnetic equator, and the high-latitude regions, including auroral zone and polar cap. The physics of equatorial ionospheric irregularities are different from those in high-latitude regions, resulting in different scintillation characteristics. Equatorial scintillations are principally associated with plasma density depletion regions formed in the bottom side of the ionospheric *F*-region during evening hours, whereas high-latitude scintillations primarily result from solar energetic particles entering the Earth's magnetosphere (near polar cusp and magnetotail neutral point) and ionosphere generating patches of plasma density irregularities along and across the magnetic field lines. In either region, scintillation has diurnal, seasonal, and annual variations which are enhanced during solar maximum.

Ionospheric plasma density irregularities—as the source of scintillation—can impair the performance of GNSS receivers though introducing unexpected phase and intensity variations to the received signals. Propagation through ionospheric irregularities, with random distribution, changes the phase modulation of the propagating signal and produces complex diffraction patterns on the ground [*Wernik et al*., 2003]. Scintillation affects GNSS receivers mostly at the tracking stage and can, therefore, corrupt the raw GNSS observations used in a variety of navigation applications. Deep signal fadings, due to intensity scintillation, and carrier wave random frequency shifts, caused by phase scintillation, can result in recurrent signal loss of lock and cycle slips in carrier tracking loops [*Klobuchar*, 1996].

Determining the performance of GNSS receivers, subject to ionospheric scintillation, is an ongoing area of research focus—particularly during the current period of solar maximum. It is useful to study scintillation impact for multiple systems, signals, and receiver characteristics through simulation. Such simulation tools can generate time series of GNSS signals which are then processed in software GNSS receiver tracking loops. The software receiver can be modeled to represent appropriate receiver characteristics (e.g., low-cost single-frequency receivers versus survey-grade multi-frequency designs). Simulation allows full control over scintillation levels and receiver design with known reference truth values. Features defining the synthetic data can be manipulated methodically to observe and isolate directly the impact of specific characteristics and assumptions. Simulation does have disadvantages in that any model assumptions or simplifications can differ from real-world conditions. In order for the simulation to be considered valid, results must be verified extensively against experimental results.

To study the impact of equatorial scintillation on GNSS signals and receivers via simulation, an ionospheric scintillation simulator is implemented following the phase screen formulation of Rino [1979, 1982, and 2011]. This model allows oblique signal propagation in an anisotropic medium with multiple irregularity layers. The model is verified through comparison with real scintillation data collected during the most recent solar maximum (mid-2012–early 2013) in equatorial region using an in-house University of Calgary 1 bit dual-channel front-end. Real data sets are exploited in post-processing to evaluate GNSS receiver performance, determine scintillation parameters, and verify scintillation simulation tools. Tracking loop performance is evaluated for the real and simulated data in terms of probability of loss of phase and frequency lock, as well as correlation of disturbed L1/L2C signals. Results confirm the effectiveness of the low-latitude scintillation simulation tools in generating real-world-like scintillation time series. The simulation model is capable of capturing the characteristics of the real-world processes in generating scintillation parameters, as their subsequent scintillated data exhibit similar stochastic behaviors, including similar power law features, variance, and probabilities.

2. Data Sets and Analysis Tools

The impact of equatorial ionospheric scintillation on Global Positioning System (GPS) signals and receivers is studied in this work using the following data sets and software/hardware analysis tools:

Real data: Real intermediate frequency (IF) samples on GPS L1/L2C frequencies are collected between June 2012 and March 2013 at IBGE (Brazilian Institute of Geography and Statistics) in Rio de Janeiro (−22°N, −43°E) using an in-house University of Calgary 1 bit dual-channel front-end with 10 MHz sampling frequency. The IF samples are post-processed using the GSNRx™ software receiver.

GSNRx™ software receiver: GSNRx™ is a GNSS software receiver, developed by the Position, Location, and Navigation (PLAN) group at the University of Calgary [*O'Driscoll et al.*, 2009]. This software is capable of processing raw GPS L1/L2/L5, GLONASS and Galileo IF samples in real time or post-mission and performs acquisition, tracking, and the computation of the navigation solution. The GSNRx™ receiver generates a number of measurements, including the signal carrier-to-noise ratio, carrier and code phase, carrier and code Doppler frequency, and loop correlator in-phase and quadraphase outputs, to name a few. Among these, the correlator in-phase and quadraphase outputs and carrier phase measurements are used to obtain scintillation parameters. This includes intensity and phase scintillation indices S_4, σ_φ in time domain, and scintillation spectral strength and spectral index (T_{scin}, ν) in frequency domain. The spectral parameters T_{scin} and ν are used to drive the scintillation simulator.

Ionospheric scintillation simulator: The scintillation simulator is implemented based on the phase screen formulation of *Rino* [1979, 1982, and 2011], which allows oblique signal propagation in an anisotropic medium with multiple irregularity layers for multiple GNSS signals. In Rino's phase screen model, it is assumed that the entire ionospheric plasma density irregularities—considered as the source of scintillation—are concentrated within a relatively thin diffracting screen at the ionospheric F_2-layer peak height (e.g., 350 km). After passing through the screen, as the wavefield propagates, the induced phase perturbations evolve and produce phase and intensity scintillations. The resulting simulated scintillation time series are modulated on simulated GPS signals (based on the Spirent GSS7700 signal simulator and the National Instruments (NI) signal generator) and processed in the GSNRx™ receiver.

Spirent GSS 7700 hardware signal generator: The Spirent hardware signal generator is capable of simulating GPS L1/L2/L5 and GLONASS L1/L2 radio frequency (RF) signals. In doing so, the simulator replicates the conditions where GNSS receivers typically operate. Analog RF signals are therefore simulated considering both the satellite-platform dynamics and atmospheric effects. A number of parameters can be set up at each data log scenario, including observable satellites, signals power level, receiver location and status (stationary versus mobile), receiver velocity, time and GPS week number, etc. [*Spirent*, 2008]. The simulated analog GNSS signals from Spirent are then amplified using an external low-noise amplifier (LNA) with approximately 30 dB gain and analyzed using the NI signal analyzer to obtain digital IF samples.

NI PXI-5660 signal analyzer: In order to filter, down-convert, and digitize the simulated analog GNSS signals, the National Instruments (NI) front-end is employed in this work. The NI front-end acquires the incoming signal

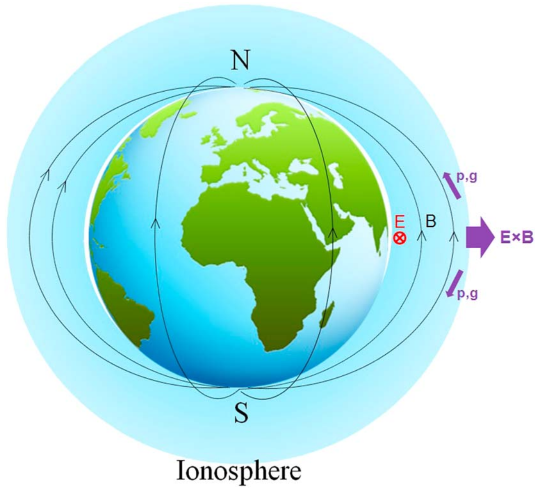

Figure 1. The ionosphere equatorial *F*-region plasma gradually moves to higher altitudes during evening hours by the upward $E \times B$ drift and eventually moves downward along the magnetic field lines due to gravity *g*, and pressure from upper layers *p*. This phenomenon, known as fountain effect, results in formation of two peaks in electron density approximately 20° either side of the magnetic equator.

with nearly 22 MHz bandwidth, down-converts the signal to IF, and samples it at 100 MHz sampling frequency. The successive digital signal is resampled in this work using a 12.5 MHz sampling frequency.

3. Low-Latitude Scintillation

Equatorial scintillations are principally associated with plasma density irregularities formed in the ionospheric *F*-region after sunset. During evening hours, the interaction between the eastward dynamo electric fields and the northward magnetic field results in an upward $E \times B$ drift (see Figure 1) which lifts the *F*-region plasma. Due to gravity and pressure from upper layers, the elevated plasma eventually moves down—along the magnetic field lines—and creates the equatorial anomaly, two peaks in electron density roughly 20° either side of the magnetic equator [*de Rezende et al.*, 2007; *Alfonsi et al.*, 2010].

As the *F*-region plasma moves to higher altitudes, the density gradient between the top and bottom side of this region increases, which, in turn, results in the formation of plasma density depletion areas, also known as plasma bubbles, in the lower *F*-region. When a bubble starts to grow or move upward, large electron density gradients on the bubble edges produce smaller irregularities. These small irregular regions with a size of the order of the first Fresnel zone radius (~260 m for the GPS L1 signal) or less can cause strong scintillations of intensity and phase of GPS signals [*Afraimovich et al.*, 2006; *Alfonsi et al.*, 2010].

3.1. Statistical Characteristics of Scintillation

Ionospheric irregularities, from which phase and intensity scintillation originates, are principally shown as perturbations δn to the local refractive index *n*, where [*Rino*, 2011]

$$\delta n = -4\pi r_e \delta N_e / k^2 \tag{1}$$

In the above equation, r_e denotes the classical electron radius (2.8198×10^{-13} cm), δN_e denotes the electron density perturbation, and *k* is the signal wave number.

Since ionospheric scintillation is the result of wave propagation in a randomly structured medium with random distribution of δn, scintillation is a stochastic process. Scintillation components can therefore be characterized using a set of statistical parameters such as mean, standard deviation, spectral density, and probability distribution function. Among these, the standard deviation and spectral density are further described below.

3.1.1. Scintillation Standard Deviation

The intensity scintillation index (S_4) and phase scintillation index (σ_φ) are generally used to determine the strength of scintillation activity. The S_4 index represents the normalized standard deviation of detrended signal intensity (SI) and is computed over 60 s intervals. The σ_φ index represents the standard deviation of detrended carrier phase and is calculated in units of radians typically over 60 s intervals to be time consistent with S_4 index.

To obtain the S_4 values, the received raw signal intensity needs to be detrended and the effect of ambient noise needs to be removed from it. Detrending the raw signal intensity measurements is accomplished in two steps: first, low-pass filtering the raw intensity measurements to remove the trend and, second, normalizing the received signal intensity to the filter output obtained in the first step. Principally, a causal sixth-order low-pass Butterworth filter with a 0.1 Hz cutoff frequency is used by researchers [e.g., *Fremouw et al.*, 1978; *Van Dierendonck et al.*, 1993] to filter the raw (typically 50 Hz) signal intensity measurements. As a more efficient alternative to this, two new data treatment algorithms are introduced in this paper which applies either a non-causal sixth-order low-pass Butterworth filter with a 0.1 Hz cutoff frequency or a cascade of six first-order low-pass Butterworth filters with a 0.2858 Hz cutoff frequency each. Details are provided in Appendix A.

After filtering the signal intensity using either of the aforementioned algorithms (non-causal or cascaded), the detrended normalized signal intensity is calculated from

$$\mathrm{SI_{det}} = \mathrm{SI}/(\mathrm{SI})_{\mathrm{LPF}} \tag{2}$$

and the corresponding (noisy) S_4 index from

$$S_{4,\mathrm{noisy}} = \sqrt{\frac{\langle \mathrm{SI}^2_{\mathrm{det}} \rangle}{\langle \mathrm{SI_{det}} \rangle^2} - 1} \tag{3}$$

For given carrier-to-noise ratio (C/N_0) level in dB-Hz, the effect of ambient noise on S_4 index can be calculated and removed via [*Van Dierendonck et al*., 1993].

$$S_4 = \sqrt{\frac{\langle \mathrm{SI}^2_{\mathrm{det}} \rangle}{\langle \mathrm{SI_{det}} \rangle^2} - 1 - \underbrace{\frac{100}{c/n_0}\left(1 + \frac{500}{19c/n_0}\right)}_{\text{effect of ambient noise}}} \tag{4}$$

where $c/n_0 = 10^{(C/N_0)/10}$.

As with the signal intensity measurements, the GPS signal carrier phase measurements need to be detrended to remove the effects of integrated Doppler due to satellite/receiver motion, satellite/user clocks, and multipath. In this work, instead of applying the typical sixth-order high-pass Butterworth filter with a 0.1 Hz cutoff frequency, a cascade of six first-order high-pass Butterworth filters, each with a 0.035 Hz cutoff frequency, is used (see Appendix A).

3.1.2. Scintillation Spectral Density

The spectral density function (SDF) of phase and intensity scintillation follows an inverse power law distribution of the form [*Rino*, 1979; *Knight and Finn*, 1998]

$$\phi(f) = \frac{T_{\mathrm{scin}}}{\left(f_0^2 + f^2\right)^{\nu}} \approx \frac{T_{\mathrm{scin}}}{f^{2\nu}} = \frac{T_{\mathrm{scin}}}{f^{p}} \tag{5}$$

where f (in Hz) represents the frequency of phase/intensity fluctuations, f_0 (in Hz) is a frequency corresponding to the ionospheric outer scale size (i.e., the size of maximum irregularity), T_{scin} (in dBrad^2/Hz) is the spectral strength at 1 Hz, and ν (unitless) is the spectral index. In *Knight and Finn* [1998], the spectral index is represented by p where $p = 2\nu$. Unlike phase scintillation, the intensity scintillation SDF is generally attenuated below a certain cutoff frequency which is a function of first Fresnel radius, the speed of signal propagation path through the irregularity regions, and the speed of irregularities within the ionosphere. The SDF given in equation (5) is usually simplified assuming $f >> f_0$ [*Rino*, 1979].

4. Scintillation Propagation Theory

Scintillation theory together with signal oblique propagation in anisotropic structured propagation media is briefly reviewed in this section. This review is based on chapters 1–4 of *Rino* [2011]. The interested reader is referred to the original book for further information.

Consider the simple case of a two-dimensional propagation medium, with x being the propagation direction, and y being the propagation transverse axis. In such system, under the weak inhomogeneity restriction for the propagation medium, the wavefield evolution in the two-dimensional space can be expressed by [*Rino*, 2011]

$$\frac{\partial \psi(x,y)}{\partial x} = \underbrace{ik\Theta\psi(x,y)}_{\substack{\text{propagation}\\\text{term}}} + \underbrace{ik\delta n(x,y)\psi(x,y)}_{\substack{\text{media-interaction}\\\text{term}}} \tag{6}$$

where $\psi(x, y)$ is the complex wavefield intensity, $i = \sqrt{-1}$ is the imaginary unit, k and δn are defined in equation (1), and Θ is the propagation operator defined in *Rino* [2011]. The general solution to this equation consists of the *media-interaction* solution plus the *propagation* solution. These two solutions can be combined in a single recursive method, known as the *split-step* algorithm introduced by *Rino* [2011]. To apply this method, the propagation medium is divided into n consecutive layers with thickness Δx_n, each layer described by local homogeneous statistical properties. Note that in Rino's work, both perturbation to local refractive index (δn) and layer number (in x_n and Δx_n) are represented by the letter n. At the beginning of each layer, the wavefront is modulated by the phase perturbation resulting from perturbation in local refractive index, and then, the wave is propagated toward the next layer using the propagation operator as given below [*Rino*, 2011]

$$\psi(x_n, m\Delta y) = \psi(x_{n-1}, m\Delta y)\,\underbrace{e^{ik\delta n(x_n, m\Delta y)\Delta x_n}}_{\text{phase perturbation}} \tag{7}$$

$$\hat{\psi}\left(x_n, l\Delta\kappa_y\right) = \sum_{m=0}^{N-1} \psi(x_n, m\Delta y)\; e^{-2\,\pi\mathrm{ilm}/N} \tag{8}$$

$$\psi(x_{n+1}, m\Delta y) = \frac{1}{N}\sum_{l=0}^{N-1}\; \hat{\psi}\left(x_n, l\Delta\kappa_y\right)\, P_l^{\Delta x_n}\; e^{2\,\pi\mathrm{ilm}/N} \tag{9}$$

According to equation (7), at the first propagation layer ($n = 1$), the initial wavefield strength $\psi(x_0, m\Delta y)$ is modulated by the phase perturbation $\exp\{ik\delta n(x_1, m\Delta y)\Delta x_1\}$. Next, in equation (8), forward Fourier transform (i.e., spatial to spectral transform) is applied to the wavefield. The result is forwarded to the next layer through multiplication with the spatial transfer function P_l defined in *Rino* [2011], and finally inverse Fourier transform (i.e., spectral to spatial) is applied in equation (9) to obtain the wavefront in spatial domain in the next layer. In equations (7)–(9), Δx_n and Δy are spatial sampling intervals and N is the size of discrete Fourier transform. These equations can simply be modified to accommodate wave propagations in three-dimensional media.

4.1. Oblique Propagation

In real world, most receivers—including GNSS receivers—collect signals from different directions, sometimes at very low elevation angles. Oblique propagation is therefore considered in the theory of scintillation to bring the simulation results closer to reality. To this aim, *Rino* [2011] has introduced a propagation coordinate system with a continuously displaced measurement plane centered on the main propagation direction.

The origin of such coordinate system is chosen to be the point where the propagating wave intersects the phase screen with downward (x_p), eastward (y_p), and southward (z_p). Propagation angle from downward axis is denoted by θ_p, and propagation azimuth angle from eastward axis is denoted by φ_p. The split-step solution (introduced in the previous section) needs to be adjusted to accommodate the oblique propagation. This starts by introducing the wavefield propagation equation in three-dimensional space as [*Rino*, 2011]:

$$\frac{\partial\psi(x,\bar{\rho})}{\partial x} = ik\Theta\psi(x,\bar{\rho}) + ik\delta n(x,\bar{\rho})\psi(x,\bar{\rho}) \tag{10}$$

where

$$\psi(x,\bar{\rho}) = \iint\left\{\hat{\psi}_{\bar{k}}(x_0,\bar{\kappa})\times\exp\left\{i\left(\mathrm{kg}\left(\bar{\kappa}+\bar{k}_T\right) - \tan\,\theta_p\hat{a}_{k_T}.\bar{\kappa}\right)\Delta x\right\}\times\exp\{i\,\bar{\rho}\cdot\bar{\kappa}\}\,\frac{d\bar{\kappa}}{(2\pi)^2}\right\} \tag{11}$$

with $\Delta x = x - x_0$, and $\bar{\rho}$ being the transverse coordinate in the displaced system. In this equation $\bar{k}$ is the constant wave number vector, defined as (after modification from *Rino* [2011])

$$\bar{k} = k\left[\cos\,\theta_p, \sin\,\theta_p\cos\,\varphi_p, \sin\,\theta_p\sin\,\varphi_p\right] \tag{12}$$

and $\hat{a}_{k_T}$ is the unit vector along the transverse component, where (after modification from *Rino* [2011])

$$\hat{a}_{k_T} = \bar{k}_T/k_T = \left[\cos\,\varphi_p, \sin\,\varphi_p\right] \tag{13}$$

In this new system, phase perturbation (the exponential term in equation (7)) is defined as [*Rino*, 2011]

$$\exp\{i\delta\varphi(x_{n+1},\bar{\rho})\} = \exp\left\{ik\,\sec\theta_p\int_{x_n}^{x_{n+1}}\delta n\left(x',\bar{\rho}+\tan\,\theta_p\hat{a}_{k_T}x'\right)dx'\right\} \tag{14}$$

The split-step solution to equation (10) can be obtained by repeating continuously the propagation and the media-interaction calculations given in equations (11) and (14).

4.2. Anisotropic Propagation Media

In a magnetized plasma (like Earth's ionosphere), charged particles tend to move along the magnetic field lines. This results in the formation of rod-shaped field-aligned anisotropic irregular regions, whose impact on propagating wavefields differs from isotropic media. The effect of anisotropic irregularities is considered

10.1002/2014RS005513

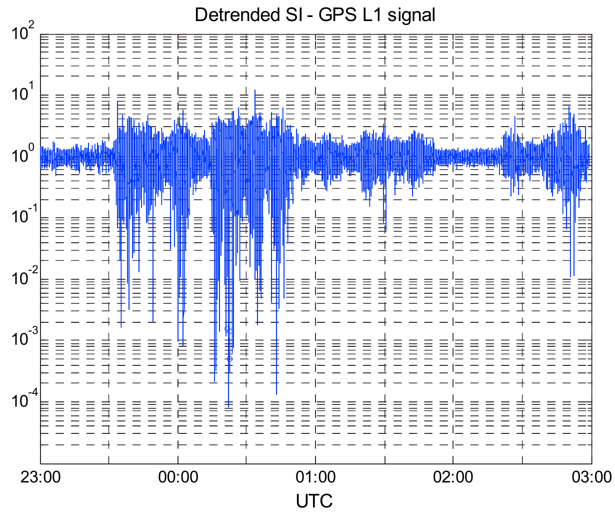

Figure 2. Detrended signal intensity for GPS L1 signal (PRN12) using the sixth-order non-causal low-pass Butterworth filter with 0.1 Hz cutoff frequency.

in the theory of scintillation via scaling and rotating the principal coordinates that initially describe isotropic structures [*Rino*, 2011]. To do this, irregularities elongation factors as well as the direction of geomagnetic field lines at any specific location within the propagation medium are required to determine the propagation medium anisotropy factors.

The general form of spectral density function (SDF) of phase and intensity scintillation—in frequency domain—is given in equation (5). Equivalent to this, for vertical propagation in an *isotopic* propagation medium, the phase scintillation SDF, which is related to the refractive index spectrum $\phi_{\delta n}(q)$, takes the following inverse power law form in spatial domain [*Rino*, 2011]

$$\phi_{\delta\varphi}(q) = k^2 l_\mathrm{p}\, \phi_{\delta n}(q) \approx \frac{k^2 l_\mathrm{p} C_\mathrm{s}}{q^{2\nu+1}} \tag{15}$$

Phase scintillation SDF is characterized by the scale-free turbulent strength parameter C_s, the signal wave number k, the scale-free spectral index ν, and irregularity layer thickness l_p. When the same wavefield is propagated *obliquely* in an *anisotropic* medium, the SDF given in equation (15) changes to (after modification from *Rino* [2011])

$$\phi_{\delta\varphi}(\overline{\kappa}) = \frac{k^2 l_\mathrm{p} C_\mathrm{s}\, ab\ \sec^2\theta_\mathrm{p}}{q^{2\nu+1}} = \frac{k^2 l_\mathrm{p} C_\mathrm{s}\, ab\ \sec^2\theta_\mathrm{p}}{\left(A\kappa_y^2 + B\kappa_y\kappa_z + C\kappa_z^2\right)^{(\nu+0.5)}} \tag{16}$$

where κ_y and κ_z are spatial frequencies, a is the principal anisotropic elongation factor and represents the irregularity dimension along the magnetic field, b is the secondary anisotropy elongation factor and represents the irregularity dimension across the magnetic field in E-W direction, and A, B, and C are anisotropy factors defined in *Rino* [2011], which are related to (a, b) and magnetic field line directions in the propagation coordinate system.

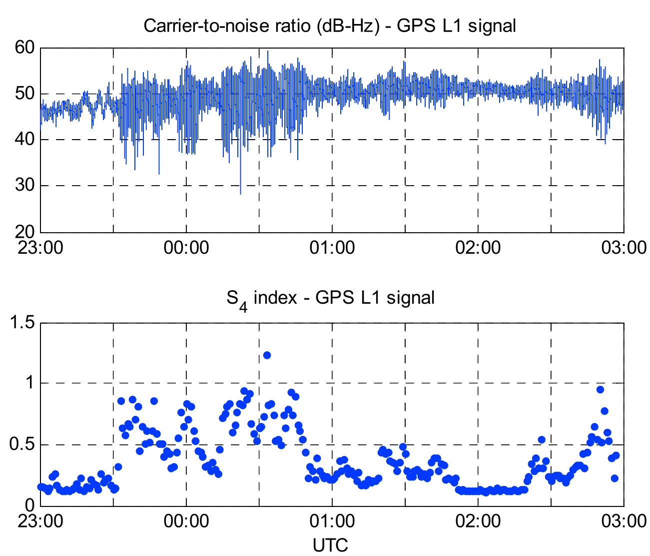

Figure 3. (top) Carrier-to-noise ratio for GPS L1 signal, PRN12 and (bottom) corresponding intensity scintillation index.

4.3. Scintillation Time Series

Since the GSNRx™ software receiver requires phase and amplitude scintillation time series, the spatial variation of the two-dimensional complex field can be converted into a function of time using [*Rino*, 2011]

$$\overline{\rho}_m = \overline{v}_k \cdot (m\,\Delta t); \quad m = 1, 2, \ldots, N_y \tag{17}$$

where m denotes the mth grid point defined on the phase screen with maximum number of points equal to N_y (see section 7 for details), $\overline{v}_k$ is the

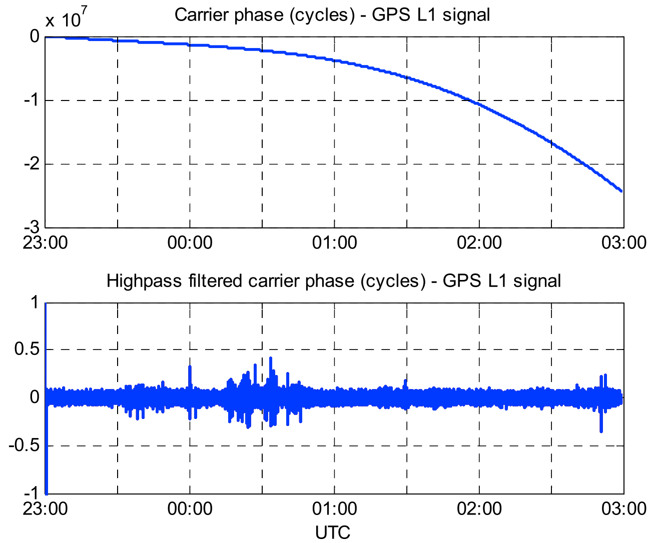

Figure 4. (top) Raw carrier phase observation (in units of cycles) for GPS L1 signal, PRN12 and (bottom) corresponding high-pass filtered carrier phase using a cascade of six first-order high-pass Butterworth filter with a 0.035 Hz cutoff frequency.

apparent velocity in the measurement plane and is a function of the drift velocity of the irregularities and the velocity of the ionospheric pierce point through the irregularity layer, and Δt is the travel time between two grid points along $\bar{v}_k$. The scintillation simulation algorithm described above is driven in this work using real scintillation data parameters. Thus, real data sets are processed first.

5. Low-Latitude Ionospheric Scintillation Characterization Using Real Data

Real IF samples, on GPS L1/L2C frequencies, are collected between June 2012 and March 2013 at IBGE (Brazilian Institute of Geography and Statistics) in Rio de Janeiro using an in-house University of Calgary 1 bit dual-channel front-end. During this period, 79 files were collected; each covers a nearly 4 h observation session from 23:00 to 03:00 in Coordinated Universal Time (UTC), corresponding to 20:00 to 00:00 (midnight) local time. The IF samples are post-processed using the GSNRx™ software receiver. Analysis of the data clearly shows a significant increase in S_4 and σ_φ values after the Fall Equinox on 22 September 2012 and a sudden decrease of these values after the Spring Equinox on 20 March 2013. The results of processing one of these files, collected on GPS satellite PRN12 during 24 and 25 October (2012), are used in this section to characterize equatorial ionospheric scintillation via calculating scintillation indices, power spectrum, and correlation level.

5.1. Scintillation Indices

Following equations (2)–(4), the 1 KHz in-phase and quadraphase channel correlator outputs are utilized to determine the signal intensity SI. The resulting 50 Hz SI values are normalized with respect to their low-pass filtered version using a *non-causal* sixth-order low-pass Butterworth filter with a 0.1 Hz cutoff frequency. The subsequent 50 Hz detrended SI values are illustrated in Figure 2 using logarithmic scale. Cascaded low-order filters (e.g., six first-order low-pass Butterworth filters with a 0.2858 Hz cutoff frequency each) are other good alternatives to the non-causal filter. The typically used causal filters, on the other hand, were not implemented in this work to avoid the phase difference between the input and output of the low-pass filter.

Substituting the detrended SI values in equation (4), and using the carrier-to-noise ratio values, the final detrended noiseless intensity scintillation index S_4 is calculated and plotted in Figure 3. According to the results shown in Figures 2 and 3, large fluctuations in signal intensity and carrier-to-noise ratio (fade depth > 15 dB) are manifested in large intensity scintillation indices ($S_4 > 0.5$).

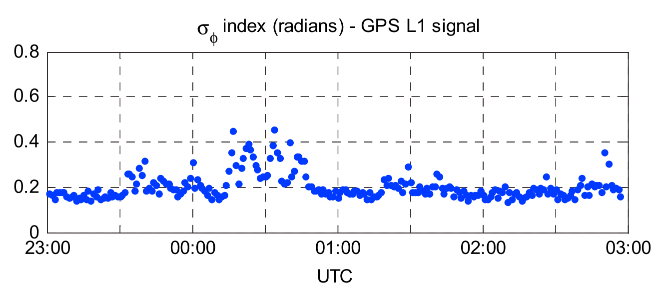

Figure 5. Phase scintillation index, in units of radians, corresponding to high-pass filtered carrier phase in Figure 4.

For the same data set, phase scintillation index is determined by high-pass filtering the 50 Hz carrier phase measurements, using a cascade of six first-order high-pass Butterworth filter with a 0.035 Hz cutoff frequency, and then, obtaining the standard deviation over 60 s intervals. Raw and high-pass filtered carrier phase, in units of cycle, is depicted in Figure 4, and the

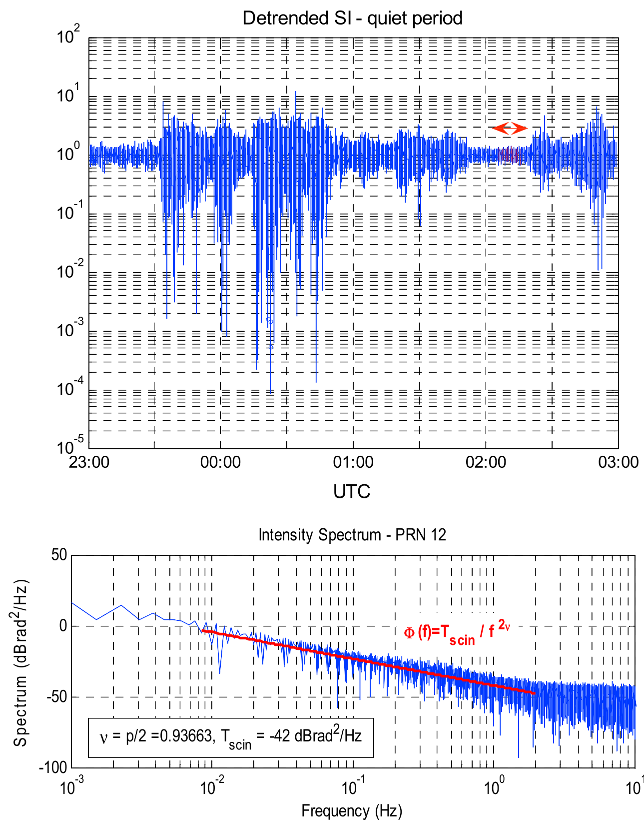

Figure 6. (top) Ten minutes of quiet intensity scintillation period in red, (bottom) corresponding power spectrum in blue and power law fitting in red for GPS L1 signal PRN12.

resulting σ_φ values, in units of radians, are illustrated in Figure 5.

Similar to the results displayed in Figure 3 for intensity scintillation, relatively large fluctuations, as large as half a cycle, are detected in the high-pass filtered carrier phase between 23:30 and 01:00 in Figure 4. This time interval corresponds to 20:30 to 22:00 local time, which is after sunset when scintillation activities are mostly expected in the equatorial region.

5.2. Scintillation Spectrum

Considering the results of intensity scintillation index S_4 in Figure 3 and carrier phase standard deviation σ_φ in Figure 5, more scintillation activities are observed during the first 2 h of data session, more specifically, from 23:30 to 1:00 UTC. To study the spectral density function (SDF) of scintillation, two data segments (10 min long each) are selected: one from a quiet time period, where scintillation activity is weak, and the other one, from the active period. For each data segment, the intensity scintillation spectrum is obtained using the detrended normalized signal intensity. The resulting intensity scintillation power spectrum is plotted in Figure 6, for the 10 min long quiet scintillation, and in Figure 7, for the 10 min long active scintillation period. Note that applying an *ideal* low-pass filter would completely eliminate all the frequencies above the cutoff frequency (here 0.1 Hz) while passing those below the cutoff, unchanged. Such ideal filter can be realized theoretically by convolution with its impulse response (i.e., sinc function) in the time domain, which requires signals of infinite extent in time. *Real* filters, for real-time applications, approximate the ideal filter via truncating/windowing the infinite impulse response. The signal truncation process automatically results in *frequency leakage*. The presence of low-frequency components (as low as 10^{-3} Hz) in the intensity scintillation power spectrum in Figures 6 and 7 is an example of such frequency leakage.

The general form of phase and intensity scintillation SDF in frequency domain is given in equation (5). To obtain the spectrum parameters T_{scin} and ν, the power law relationship given in equation (5) needs to be linearized as follows [*Zhang et al.*, 2010]:

$$10\,\log_{10}(\phi(f)) = 10\,\log_{10}(T_{\text{scin}}) - 20\nu\log_{10}(f) \tag{18}$$

Selecting m data points from the linear section of power spectrum, the linearized power law equation can be rearranged into the matrix format of

$$Z = XY \tag{19}$$

where

$$X = \begin{bmatrix} 1 & -20\,\log_{10}(f_1) \\ 1 & -20\,\log_{10}(f_2) \\ \cdots & \cdots \\ 1 & -20\,\log_{10}(f_m) \end{bmatrix}, \quad Y = \begin{bmatrix} 10\,\log_{10}(T_{\text{scin}}) \\ \nu \end{bmatrix}, \quad Z = \begin{bmatrix} 10\,\log_{10}(\phi(f_1)) \\ 10\,\log_{10}(\phi(f_2)) \\ \cdots \\ 10\,\log_{10}(\phi(f_m)) \end{bmatrix} \tag{20}$$

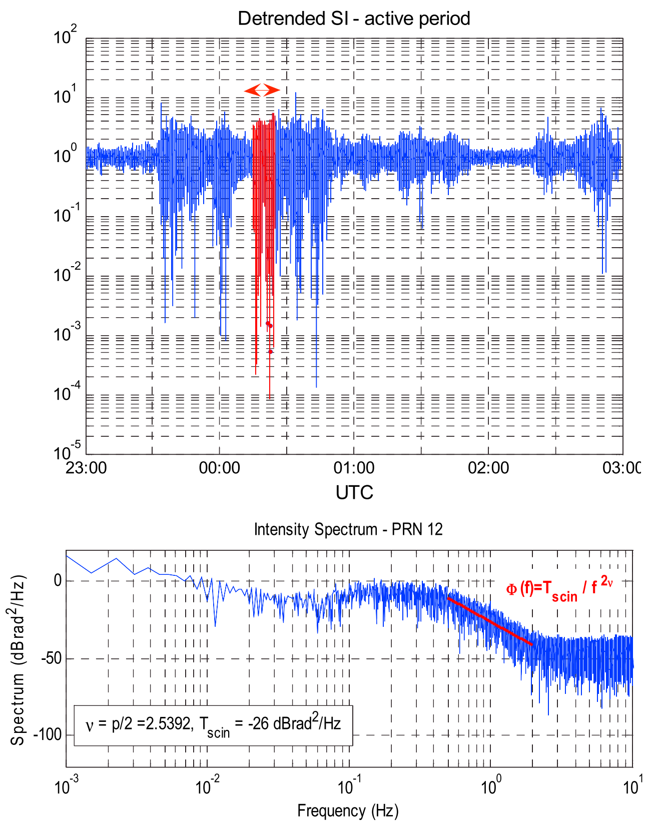

Figure 7. (top) Ten minutes of active intensity scintillation period in red, (bottom) corresponding power spectrum in blue and power law fitting in red for GPS L1 signal PRN12.

The two unknowns T_{scin} and ν can therefore be obtained from the linear least squares algorithm given in the following equation.

$$Y = \left(X^T X\right)^{-1} X^T Z \tag{21}$$

Following this method, the linearly fitted power law spectrum is calculated for the linear segment of power spectrum of each signal and is depicted with a solid red line, along with the power spectrums, in Figures 6 and 7. Considering these two figures, the strength of the intensity spectrum at 1 Hz frequency is found to be $T_{scin} = -42$ dBrad^2/Hz for quiet period, and $T_{scin} = -26$ dBrad^2/Hz for active period. In this context, a larger T_{scin} value is an indicator of a stronger scintillation activity. Consequently, the GPS L1 signal experiences much stronger fluctuations (or signal fadings) during the active scintillation period. The same conclusion can be drawn from the results of intensity scintillation index S_4 shown in Figure 3 where it specifies a higher intensity scintillation level for the first 2 h of data set. To determine the spectral density function of phase scintillation, one can simply repeat a similar process for detrended high-pass filtered carrier phase measurements given in Figure 4.

5.3. Scintillation Correlation

The principal purpose of this section is to determine the relationship between the scintillation-induced intensity and phase fluctuations of two GPS signals (here L1 and L2C) as they pass through the same region of ionospheric irregularities.

Detrended intensity scintillation time series obtained for L1 and L2C signals is plotted in Figure 8 (top). The corresponding intensity scintillation correlation level, calculated over 1 min intervals, together with intensity scintillation index S_4 for each signal is given in Figure 8 (middle and bottom), respectively. The GSNRx™ software receiver supports L2C tracking for both L2CM (civil moderate length) and L2CL (civil long) ranging codes. The results of processing L2CM signal are selected for display in this paper.

As shown in Figure 8, at low S_4 values (i.e., $S_4 \leq 0.2$), the correlation coefficient between GPS L1 and L2CM signal intensity is very low, varying mostly between ± 0.3. In the absence of scintillation, the receiver thermal noise becomes a major source of fluctuation in signal intensity, and since it is uncorrelated between the two signals, it results in low correlation values. During moderate to strong scintillation periods, however, the correlation between L1 and L2CM signal intensity seems to be fairly high. A good question would be *is the signal intensity correlation level a monotonic function of scintillation strength*? To find an answer, the correlation level between L1 and L2CM signal intensity, calculated over 1 min intervals, is plotted versus S_4 (calculated on L1 signal) in Figure 9 (top). Figure 9 (bottom) demonstrates the correlation level between the L1 and L2CM intensity scintillation indices, depicted as S_4 (L1) and S_4 (L2CM), during weak to strong scintillation periods. Same as Figure 8, the S_4 indices and correlation coefficients shown in Figure 9 are calculated for the entire 4 h long data set.

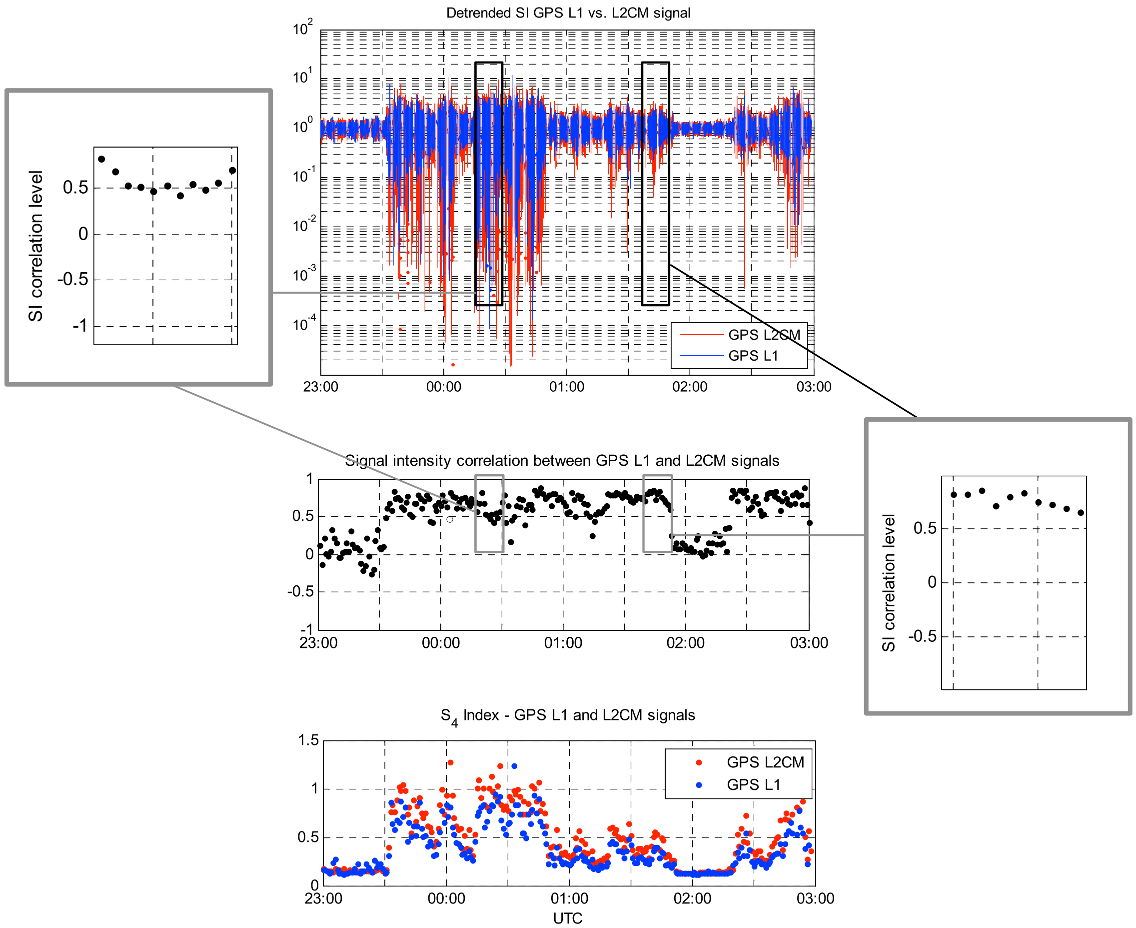

Figure 8. (top) Detrended intensity scintillation for GPS L1 and L2CM signals for PRN12, (middle) intensity scintillation correlation level calculated over 1 min intervals, and (bottom) intensity scintillation index.

As illustrated in Figure 9 (top), during weak scintillation periods, marked as region (1) in the figure with $S_4 \leq 0.2$, there is no correlation between the two signals due to the impact of receiver thermal noise. On the other hand, relatively high correlation values (i.e., 0.6 to 0.9) are observed in region (2) where $0.2 \leq S_4 \leq 0.4$. Afterward, in region (3), the correlation values tend to scatter randomly with a light decreasing trend as S_4 increases beyond 0.4. This plot indicates that there is no monotonic relationship between signal intensity correlation level and scintillation strength in general. A very similar pattern as of Figure 9 (top) is obtained earlier for L1/L2 signal correlation versus S_4 index by *Carrano et al.* [2012].

Under weak scatter conditions [*Rino*, 1979], the S_4 index obtained on the GPS L2 frequency is about 1.45 times the S_4 index obtained on L1 [*Conker et al.*, 2003]. Depicted in Figure 9 (bottom) are the intensity scintillation indices calculated from processing real scintillation data. Our results show that real data follows the theoretical predictions only at moderate scintillation level with $0.2 \leq S_4 \leq 0.5$. The $S_4(L2) = 1.45\ S_4(L1)$ relationship is violated when weak scatter conditions for L2 are violated. For the whole data set, S_4 (L2) is obtained to be 1.25 times the S_4 (L1) as shown in Figure 9 (bottom).

The same process is repeated for detrended carrier phase measurements. The high-pass filtered detrended carrier phase on L1 and L2CM, along with phase correlation and phase scintillation index σ_φ, is illustrated in Figure 10. Unlike intensity scintillation, the effect of receiver thermal noise on phase scintillation is negligible; thus, the phase correlation between L1 and L2CM is very high during weak phase scintillation activities. As phase fluctuation increases (corresponding to $\sigma_\varphi > 0.25$ radians in Figure 11), the phase scintillation correlation values tend to scatter randomly while showing a decreasing trend.

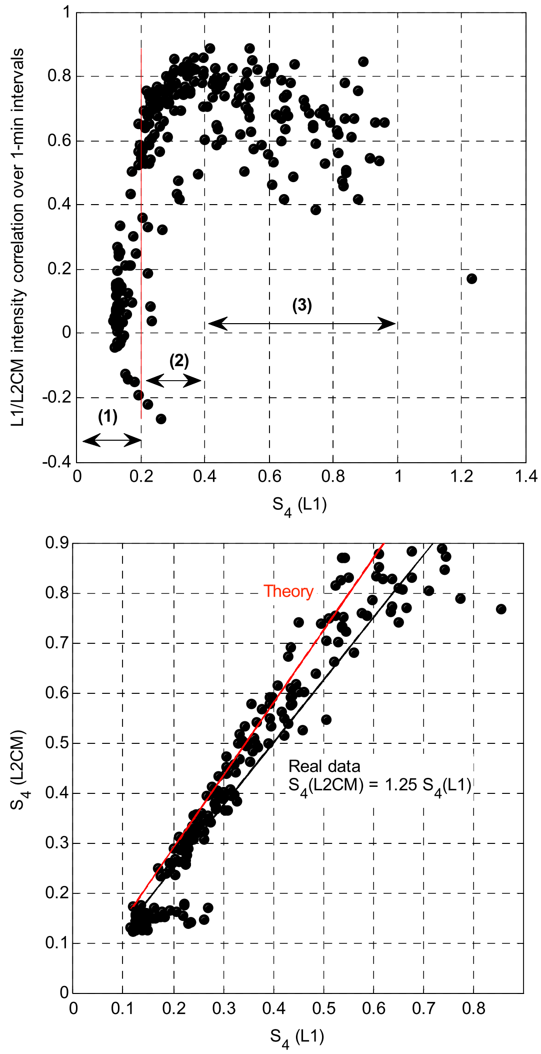

Figure 9. (top) Correlation level between L1 and L2CM signal intensity versus S4(L1) and (bottom) correlation between S4(L1) and S4(L2CM) indices. The S_4 indices and correlation coefficients shown in the plots are calculated for the entire 4 hour long data set.

6. Scintillation Impact on GNSS Receivers

Deep signal fades, as a result of signal intensity scintillation, can affect the acquisition stage of a typical GNSS receiver; in extreme cases, the receiver is unable to detect/acquire the scintillated signal. If a signal has been acquired successfully, the scintillation-induced fades and carrier phase fluctuations can cause recurring signal loss of lock in the tracking stage; hence, the receiver may be forced into reacquisition mode. In the following section, the impact of real scintillation data on the frequency and phase locked loop of a high-end GNSS receiver (GSNRx™ software receiver) is investigated.

6.1. Carrier Frequency/Phase Loss of Lock

In the GSNRx™ software receiver, the carrier tracking algorithm starts using a wide FLL (frequency-locked loop), of second order with 8 Hz bandwidth, specifically designed to have a large pull-in region and determine itself if it has locked. If the FLL has locked (determined via frequency lock indicator, FLI), the tracking algorithm moves to a narrower FLL, which will allow longer integration periods. If the FLI is high enough, tracking moves to an FLL-assisted DLL (delay-locked loop) tracker which uses lower FLL bandwidth of 6 Hz, otherwise, reverts to the previous method (FLL-DLL). At this stage, if frequency is being tracked well enough (i.e., FLI is high enough), the tracking loop attempts to track phase also using a third-order loop and 15 Hz bandwidth. But if not (i.e., very low FLI), it reverts to previous FLL-DLL. If the phase is tracking well (sufficiently high phase lock indicator, PLI), tracking transition would be toward PLL-DLL. If the phase is stable enough (very high PLI), tracking algorithm moves to a narrower PLL-DLL which again allows longer integration periods.

The frequency and phase lock indicators, FLI and PLI, are two parameters typically used in receivers to determine whether or not a signal is being tracked effectively. Both parameters are calculated using in-phase (I) and quadraphase (Q) channel correlator outputs. Accordingly, the frequency lock indicator is determined via [*Mongredien et al.*, 2006]

$$\mathrm{FLI}_k = \frac{\left(I_{k-1}I_k + Q_{k-1}Q_k\right)^2 - \left(I_{k-1}Q_k - I_kQ_{k-1}\right)^2}{\left(I_{k-1}I_k + Q_{k-1}Q_k\right)^2 + \left(I_{k-1}Q_k - I_kQ_{k-1}\right)^2} = \cos\left(4\pi\delta f_k T_{\mathrm{coh}}\right) \tag{22}$$

where k and $k-1$ represent two adjacent measurement epochs, δf is the frequency error (frequency difference between the incoming signal and its replica generated by the receiver), and T_{coh} is the coherent integration time.

The phase lock indicators is computed from [*Van Dierendonck*, 1996]

$$\mathrm{PLI}_k = \frac{{I_k}^2 - {Q_k}^2}{{I_k}^2 + {Q_k}^2} = \cos\left(2\delta\varphi_k\right) \tag{23}$$

where $\delta\varphi$ is the phase error (phase difference between the incoming signal and its replica generated by the receiver).

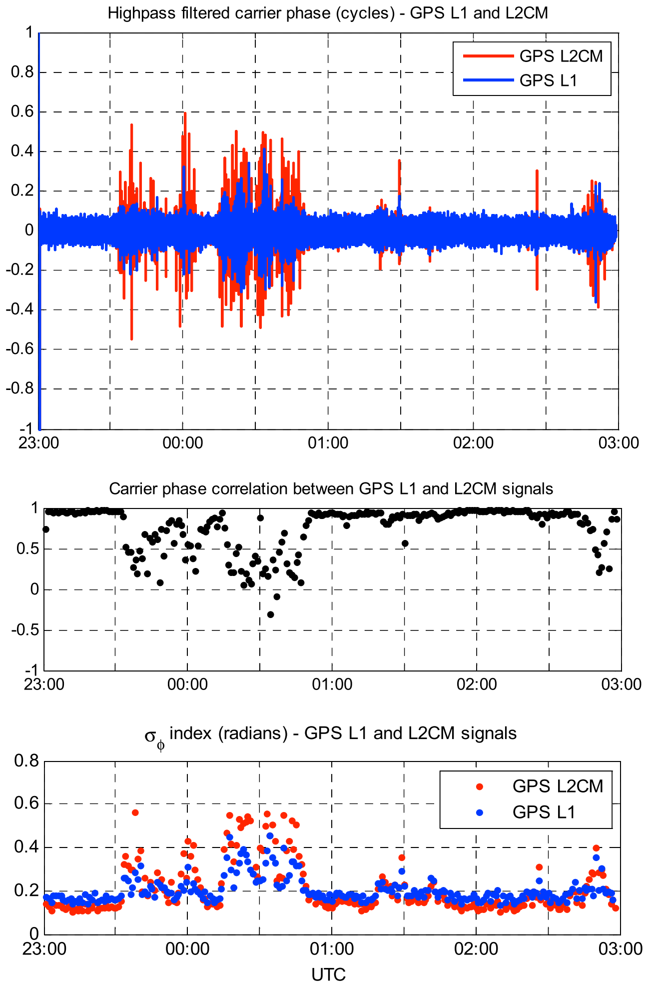

Figure 10. (top) Detrended high-pass filtered carrier phase on L1 and L2CM signals, (middle) phase scintillation correlation calculated over 1 min intervals, and (bottom) phase scintillation index in radians.

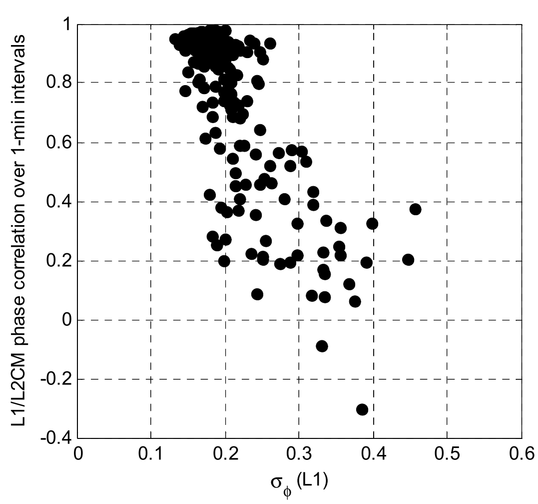

Figure 11. Correlation level between GPS L1 and L2CM detrended high-pass filtered carrier phase versus phase scintillation index in radians.

The FLI and PLI values range between −1 (worst case) and +1 (best case). In the GSNRx software receiver, the FLI and PLI lock and loss of lock thresholds are considered as follows: (i) frequency lock threshold = 0.95, (ii) frequency loss of lock threshold = 0.20, (iii) phase lock threshold = 0.9, (iv) phase loss of lock threshold = 0.60, (v) tight phase lock threshold = 0.95, and (vi) tight phase loss of lock threshold = 0.75.

In the GSNRx™ software receiver, the default threshold for phase loss of lock is set to 0.6. This value corresponds to $\delta\varphi \approx 25°$ phase error between the incoming signal and its replica generated by the receiver, following equation (23). Using the more conservative phase difference of $\delta\varphi = 15°$ (PLI = 0.86) is very common among researchers in this field (see, for example, *Knight and Finn* [1998] and *Jwo* [2001]). For the aforementioned lock and loss of lock thresholds, the FLI and PLI values are calculated during the 4 h data tracking session and depicted in Figure 12. As can be seen from the figure, during the first 2 h of tracking, where signal experiences extensive intensity and phase fluctuations due to scintillation effects, frequency and phase loss of lock occur for several epochs. The horizontal line in each plot represents the loss of lock threshold. In Figure 12 (bottom), the periods where phase lock indicator exceeds the 0.6 threshold level are shown in red circles. For each period, the probability of loss of phase (P_{loss}) along with the average intensity scintillation index (S_4) and the signal carrier-to-noise ratio (as a reference) are given in Figure 13. For all three cases, the S_4 index is about 0.7 which represents a strong scintillation level. For the more general threshold of PLI = 0.86 (corresponding to $\delta\varphi = 15°$), the probability of loss of phase (P_{loss}) increases more than fivefold as given in Figure 13.

The same process is repeated for GPS L2CM signal, PRN 12. The resulting FLI and PLI are plotted in Figure 14. In order to compare the probability of loss of phase (P_{loss}) on GPS L1 versus L2CM signal, the same periods as of Figure 13 are used to calculate the P_{loss} on L2CM. The subsequent probability values are given in Figure 14 for two different threshold levels 0.6 and 0.86.

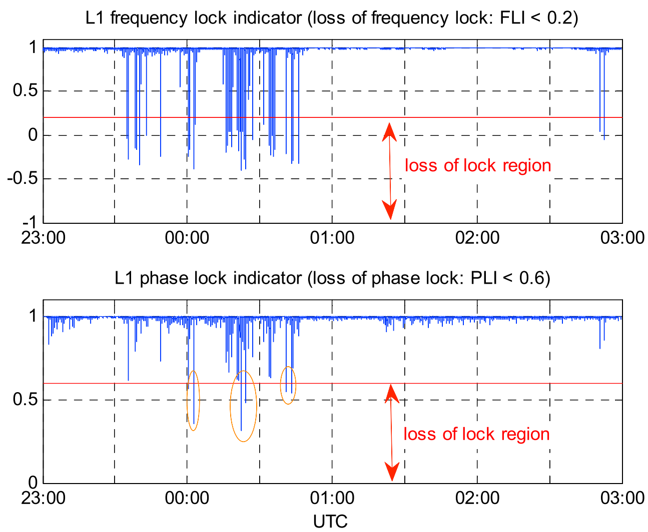

Figure 12. (top) Frequency lock indicator with loss of frequency lock for FLI < 0.2 and (bottom) phase lock indicator with loss of phase lock for PLI < 0.6.

Even though the probability of loss of phase lock is negligible for both L1 and L2CM signals in the GSNRx™ software receiver, the results shown in Figures 12–14 provide interesting information: frequency loss of lock occurs more frequently compared to phase loss of lock. Moreover, the same scintillation scenario has more destructive impact on L2CM signal compared to L1 signal with $P_{loss,L2CM} \approx 3 \times P_{loss,L1}$. This is probably due to the fact that L2CM is ~ 4.5 dB weaker than L1. And finally, there is a direct relationship between the strength of scintillation and loss of phase/frequency lock. Based on our results, loss of phase on GPS L1 signal occurs when $S_4 \geq 0.7$. In addition to fading depth (quantified by S_4), the fading rate (quantified by the decorrelation time) is also a key factor in causing loss of phase lock in GNSS receivers as demonstrated by *Carrano and Groves* [2010]. Fading rate is related to both the perturbation strength and the effective velocity with which the signal propagation path scans through the ionospheric irregularities—the effective velocity differs for each satellite pass. As shown in *Carrano and Groves* [2010], under similar ionospheric conditions (where similar S_4 index is measured), the number of loss of lock events varies among different satellites; an increased number of loss of lock events is associated with the higher fading rate.

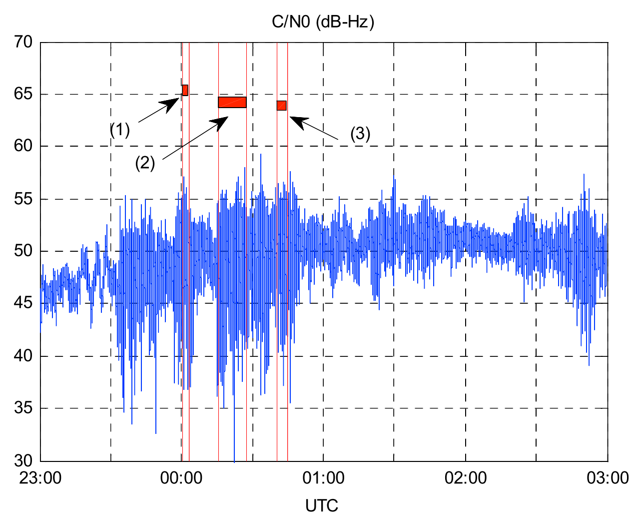

region	1	2	3
Duration (minutes)	3	10	4
$\mathbf{S_4}$	0.7	0.7	0.7
$\mathbf{P_{loss}(\%), PLI = 0.6}$	0.12	0.1	0.06
$\mathbf{P_{loss}(\%), PLI = 0.86}$	0.52	0.68	0.51

Figure 13. Carrier-to-noise ratio for GPS L1 signal, PRN12. For each time segment shown on the plot, the time duration, the average S_4 index, and the probability of loss of phase lock are given in the table.

7. Scintillation Simulator

To generate synthetic scintillation data sets, the phase screen model introduced in *Rino* [2011] is implemented. The signal transmitter is considered to be the GPS satellite PRN3. For this satellite, the set of two-line elements (TLE) corresponding to 5 April 2011 is obtained from North America Aerospace Defense Command website and provided as input to the simulator. The satellite PRN number and the date are selected arbitrarily.

The phase screen is assumed at 350 km altitude (i.e., maximum F_2-layer height), and a *virtual* ground station is considered in the equatorial region at −22°N, −43°E,

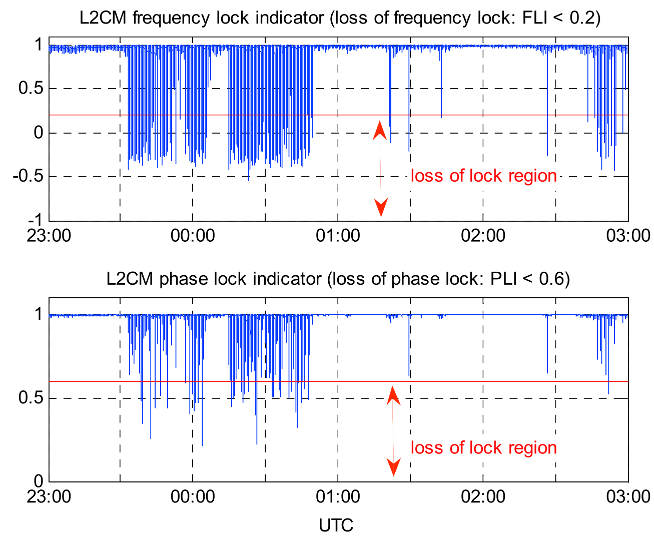

region	1	2	3
$P_{loss}(\%)$, PLI = 0.6	0.32	0.31	0.19
$P_{loss}(\%)$, PLI = 0.86	1.75	2.31	1.97

Figure 14. For the three periods shown in Figure 13, the probability of loss of phase lock is given for GPS L2CM signal assuming PLI = 0.6 (GSNRx™ default setting) and PLI = 0.86 (typical threshold).

and 100 m altitude, same coordinates as of Rio de Janeiro where our real data were collected. Following *Rino* [2011], the Simplified General Perturbation (SGP4) model is used to determine the state vector (i.e., position and velocity time series) of the GPS satellite. Having the satellite's state vector, together with the height of phase screen and receiver's location, the propagation angles (θ_p, φ_p) are calculated (details are provided in Appendix A). The coordinates of the ionospheric pierce point (IPP), where the propagating wave intersects the phase screen, are used in the International Geomagnetic Reference Field model [*Finlay et al.*, 2010; *Rino*, 2011] to determine the direction of magnetic field lines within the propagation coordinate system introduced in section 4.1. In the simulation, the principal and secondary anisotropy elongation factors are set to $a = 10$ and $b = 1$; typical numbers for the equatorial region.

To simulate different scintillation realizations, the propagation medium, from 350 km altitude to the surface, is divided into $n = 15$ phase perturbation screens. The scintillation simulator initializes the two-dimensional wavefield $\psi_{(N_y \times N_z)}(x_0, y, z)$ with all-one values just before it passes through the phase screen assuming $N_y = N_z = 2^{13}$ grid points and 10λ grid spacing with λ being the signal wavelength. The phase perturbation, given in equation (14), is then modulated on the wavefront at the screen height and the wave is propagated toward the next layer using the split-step algorithm. The process is repeated for the subsequent layers until the wavefield reaches the receiver antenna.

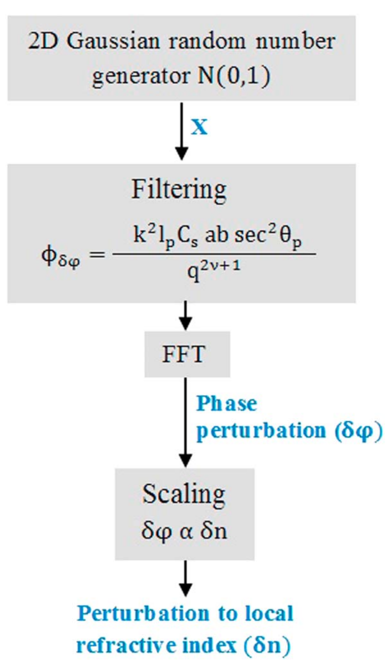

Figure 15. Generating the two-dimensional profile of index of refraction perturbation.

The two-dimensional phase perturbation profile (at nth layer with $n = 1, 2, \ldots, 15$) is generated by means of a Gaussian random number generator (see Figure 15), in the form of

$$X_{(N_y \times N_z)}(x_n, y, z) = \left(R_n(N_y, N_z) + i * R_n(N_y, N_z)\right)/\sqrt{2} \qquad (24)$$

where R_n represents the random number generator function in MATLAB. A spatial filtering process takes the fast Fourier transform of the $X_{(N_y \times N_z)}$ values after being rescaled by the filter response amplitude corresponding to the phase perturbation SDF given in equation (16). The simulator then applies a scaling factor to the resulting phase perturbation $\delta\varphi_{(N_y \times N_z)}$ profile to obtain the profile of refractive index perturbation $\delta n_{(N_y \times N_z)}$ given in equations (15) and (16).

In this work, the spectrum parameters T_{scin} and ν of real ionospheric scintillation events—obtained in section 5.2—are used to drive the scintillation simulator. This is done by substituting the power spectral index ν directly in equation (16) and using the relationship between

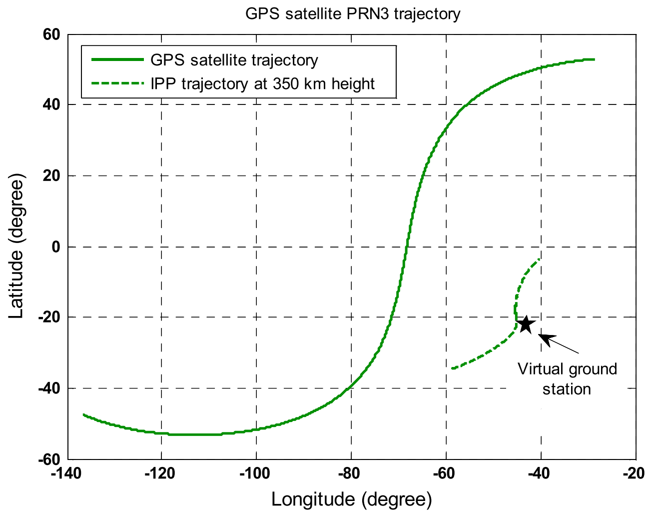

Figure 16. GPS PRN3 and its 350 km intersect point trajectory.

the turbulent strength parameter C_s (in equation (16)) and the scintillation spectral strength T_{scin} given in *Rino* [2011]

$$C_s = \frac{(2\pi)^{2\nu+1}\Gamma(\nu+0.5)\sqrt{AC - B^2/4}T_{scin}}{ab\ v_{eff}k^2 l_p \sec^2\theta_p\sqrt{\pi}\Gamma(\nu)} \tag{25}$$

with v_{eff} being the effective velocity of the signal propagation path through the ionospheric irregularity layer. Following Rino's scintillation model and using real scintillation spectral density parameters, several scintillation scenarios are simulated. Examples are given in the following sections.

7.1. Scintillation Time History

As mentioned earlier, the GPS satellite PRN3 is considered as the signal transmitter in this work. This satellite is visible from our virtual ground station (considered in Rio de Janeiro at −22°N, −43°E) for few hours on 5 April 2011. The satellite trajectory is shown in Figure 16. The entire satellite observation period is divided into paths of 40 s long, and along each individual path the wavefield propagation is simulated assuming $n = 15$ refraction layers with the phase screen at 350 km altitude. The satellite path length and the number of refraction layers are selected arbitrarily. The recorded phase (in units of radians) and intensity (in dB) for one of this passes is given in Figure 17 assuming $\nu = 1.33$ and $C_s = 10^{19}$ ($\approx T_{scin} = -35$ dBrad^2/Hz). To obtain phase and intensity scintillation time series, as of Figure 17, the spatial variation of the simulated two-dimensional complex field is converted into a function of time by substituting the apparent velocity v_k in equation (17); see Appendix A for details.

The simulated scintillation signal in time domain can be represented in the general form of $S_{scin}(t) = \sqrt{I_s(t)}$ $\exp\{j\theta_s(t)\}$, with $I_s(t)$ and $\theta_s(t)$ being the intensity and phase scintillation signals, respectively. As depicted in Figure 18, the simulated phase and intensity scintillation records are modulated on the simulated GPS L1 signal (based on Spirent Signal Generator), using complex modulation algorithm. The subsequent scintillated GPS signal is then processed in the GSNRx™ software receiver.

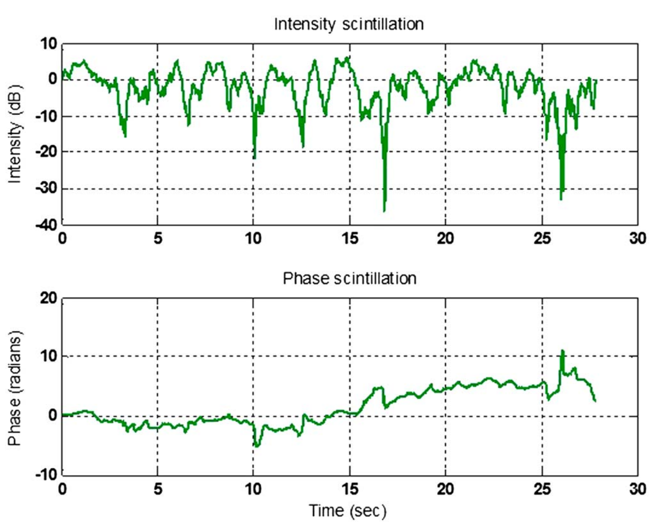

Figure 17. Simulated scintillation time series using Rino's scintillation model simulator.

7.2. Scintillation Simulation Using Real Data Parameters

The results of processing real scintillation data in frequency domain is depicted in Figures 6 and 7. The power spectrum parameters, including spectrum index ν and power spectrum strength T_{scin}, are used to drive the scintillation simulation algorithm. Using $\nu = 0.93$ and $T_{scin} = -42$ dBrad^2/Hz, given in Figure 6, a number of weak scintillation time series are simulated. To give an example, nearly 30 s of a simulated weak scintillation scenario is shown in Figure 19 (top) with the corresponding power spectrum (bottom).

To simulate strong scintillation scenarios, the scintillation parameters in Figure 7 are used. Accordingly, for $\nu = 2.5$ and

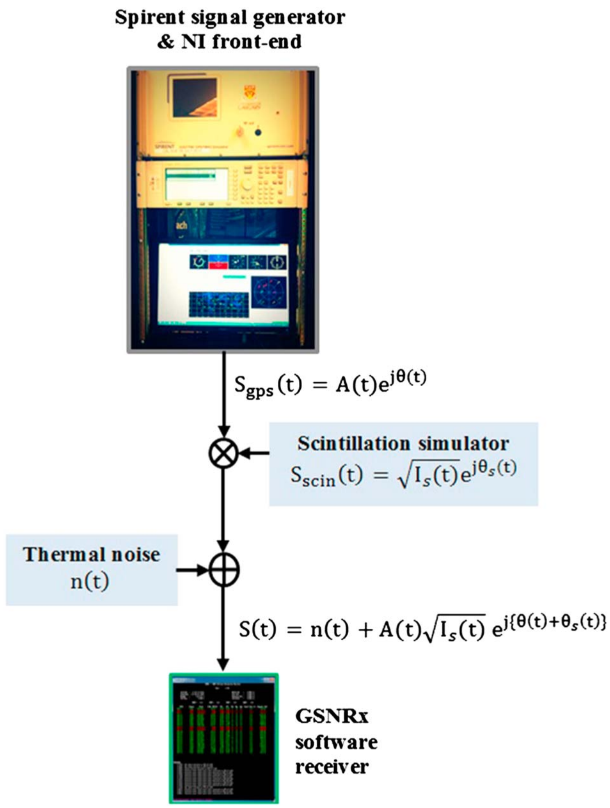

Figure 18. Scintillation simulation methodology. The synthetic phase and intensity scintillation record $S_{scin}(t)$ is modulated on the simulated GPS L1 signal $S_{gps}(t)$ using complex modulation algorithm. After adding thermal noise $n(t)$, the resulting scintillated noisy GPS signal $S(t)$ is processed in the GSNRx™ software receiver.

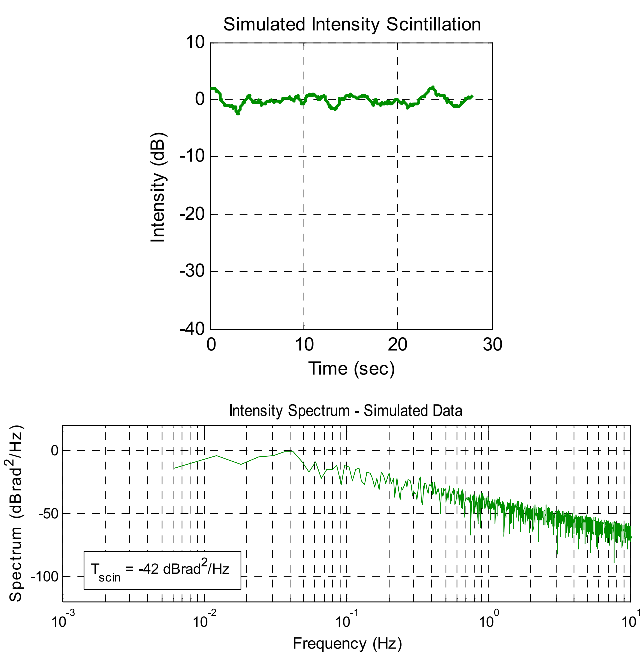

Figure 19. (top) Simulated weak intensity scintillation signal using Rino's model and (bottom) corresponding power spectrum.

$T_{scin} = -26$ dBrad^2/Hz, several strong scintillation time series are simulated. One example of such simulation results is given in Figure 20.

Repeating this procedure, 10 min of weak and strong synthetic scintillation data is simulated. Scintillation signals are modulated on simulated GPS L1 signal and processed in the GSNRx™ software receiver. The results of simulated *strong* scintillation signals are selected for display in this paper.

7.3. Scintillation Model Verification

The results of processing real and synthetic scintillation data sets are shown in this section. Figure 21 shows nearly 10 min long detrended signal intensity (SI) of two active scintillation periods. Figure 21 (top) is the result of processing real data, shown earlier in Figure 7, and is given here as a reference. Figure 21 (bottom) is the result of simulation, where 10 min long simulated strong scintillation is modulated on 30 min long GPS signal between minutes 10 and 20.

In Figure 21, the difference between the detrended intensity scintillation signal obtained from real data and the one obtained from simulation tools lies in the seeding/constructing source of each signal. In real-world scintillation scenarios, an arbitrarily selected period of strong scintillation typically includes some epochs of moderate or weak scintillation in between, which results from wave propagation in a *randomly structured* propagation medium (here the ionosphere). To generate the synthetic scintillation signal, the characterizing parameters of the real signal (ν, T_{scin}) are extracted and fed as input to a *random signal* generator. Due to the nature of random signals, the output of the scintillation simulator would be essentially different in details from the real signal (or from any other random signal) despite the fact it preserves the overall characteristics of the input real signal. Accordingly, the *overall* behavior of the simulated scintillation signals is of importance (not their details), and used in this work to verify the scintillation

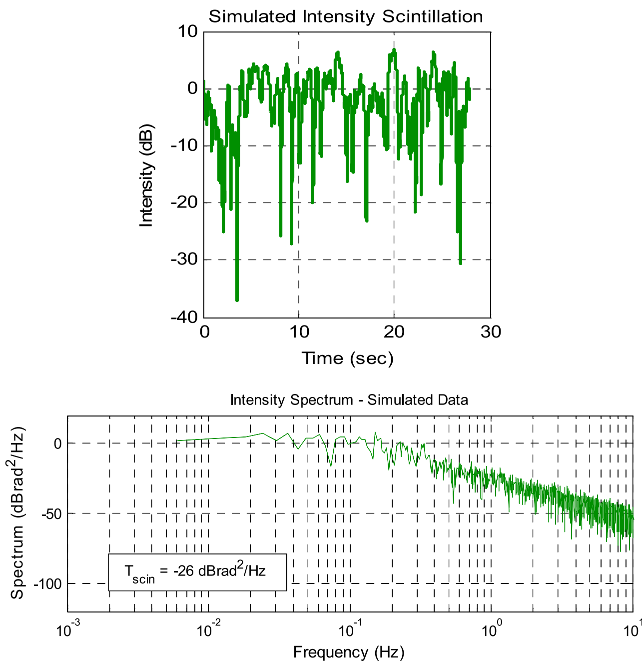

Figure 20. (top) Simulated strong intensity scintillation signal using Rino's model and (bottom) corresponding power spectrum.

simulation model. The performance of such simulated scintillation signals can be evaluated, for instance, in terms of signal variance (which utilizes block processing rather than epoch to epoch), and the probability of a certain behavior, such as impact on GNSS tracking loops.

To verify the effectiveness of the implemented simulation model in generating real-world-like scintillation scenarios, the results of calculated intensity scintillation index S_4 and real versus simulated scintillation impact on the GSNRx™ software receiver are compared in this section. For the signals shown in Figure 21, the corresponding intensity scintillation index S_4 is calculated and illustrated in Figures 22. For both signals, the S_4 index varies between 0.6 and 1. The average S_4 value over the entire 10 min interval is 0.74 for real data and 0.8 for simulated signal. The difference between the average S_4 values is less than 0.1.

To investigate the impact of real and simulated scintillation signal on the performance of the GSNRx™ software receiver, the results of calculated PLI are depicted for real data in Figure 23 (top) and for simulated signal in Figure 23 (middle). As before, 0.6 is assumed to be the threshold for loss of phase lock in the receiver. Since PLI is calculated by GSNRx™ every 20 msec, it is not easy to visually determine the number of epochs with PLI < 0.6 from Figure 23 (middle). For this, Figure 23 (middle) is zoomed in (between minutes 12 and 13) for clarification. The result is shown in Figure 23 (bottom). For the plots displayed in this figure, the probability of loss of phase lock (P_{loss}) is calculated as %0.10 for real data and %0.19 for simulated signal. The values are close for both signals and negligible in general, indicating the good performance of the GSNRx receiver under scintillation activities.

The comparison between the results of processing synthetic scintillation and those obtained from processing real data (collected on 24 and 25 October 2012, and several other data sets processed by the authors for this study) confirms the effectiveness of the scintillation simulation algorithm in generating real-world-like scintillation time histories. In other words, the simulation model introduced by *Rino* [2011] is capable of capturing the characteristics of the real-world processes in generating scintillation parameters, as their subsequent scintillated data exhibit similar stochastic behaviors, including similar power law features, standard deviations (here intensity scintillation index S_4), and probabilities (here probability of loss of phase lock).

8. Summary and Conclusion

Obtaining an appropriate scintillation simulation model with capability to generate realistic scintillation scenarios at all different scintillation levels is valuable, especially in the years following the current solar maximum, as the number of real scintillation events would probably drop. For this purpose, a number of equatorial region data sets, collected between June 2012 and March 2013, are exploited in post-processing to develop realistic simulation tools and evaluate GNSS signals, as well as GNSS receiver performance. The scintillation simulator implemented/verified in this work is based on the phase screen formulation of *Rino* [2011]. The principal features of this model are that (i) it allows both vertical and oblique signal propagation in anisotropic propagation media, (ii) it can be implemented for multiple GNSS frequencies, and (iii) multiple irregularity layers can be applied in the simulation algorithm. The observed real scintillation parameters are used to drive the simulation model.

 10.1002/2014RS005513

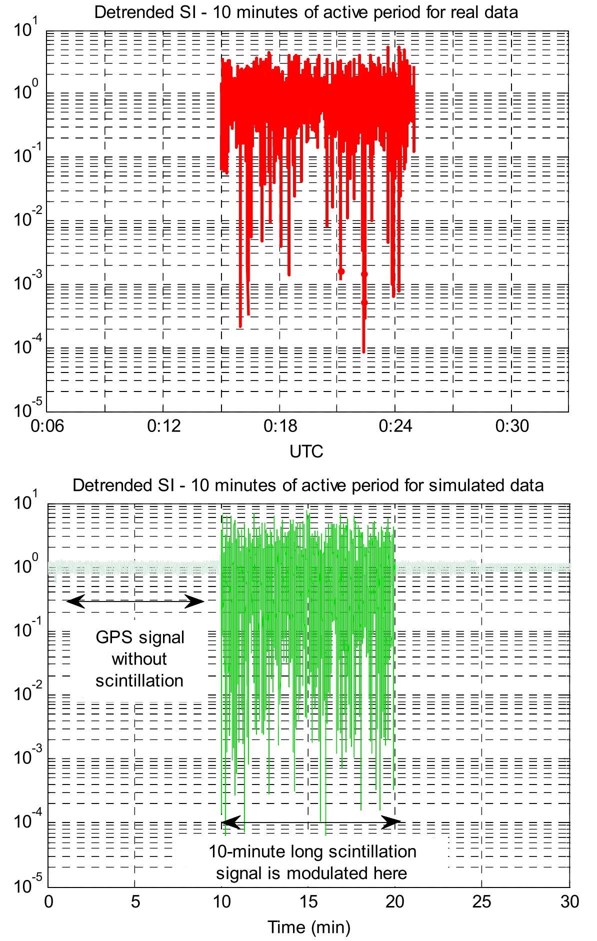

Figure 21. Ten-minute long detrended intensity scintillation signal selected from (top) real data set and (bottom) scintillation simulator. The real data displayed in Figure 21 (top) is collected on GPS satellite PRN12 on 25 October (2012) between 0:15 and 0:25 UTC and is part of the plot shown earlier in Figure 7. The 10 min long simulated strong scintillation signal shown in Figure 21 (bottom) is modulated on the 30 min long GPS signal PRN3 between minutes 10 and 20.

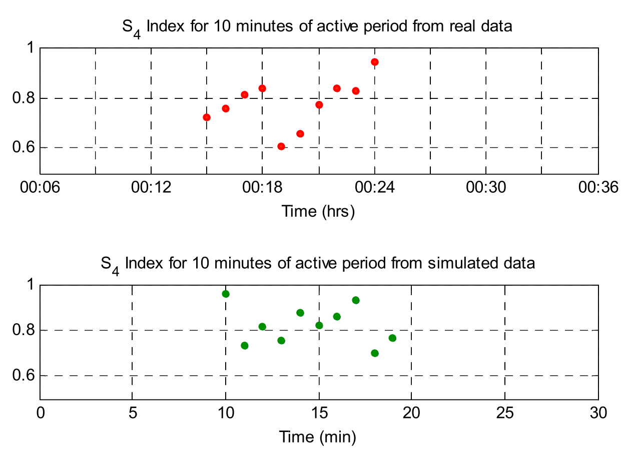

Figure 22. Intensity scintillation index S_4 calculated from the detrended intensity scintillation signal shown in Figure 20 for (top) real data and (bottom) simulated signal.

The subsequent simulated GNSS signal time series are then verified through comparison with real data for both weak and strong signal tracking scenarios. Using both real and synthetic data sets, the impact of scintillation on observation quality and receiver performance is evaluated in terms of carrier-to-noise ratio level, probability of phase, and frequency loss of lock, as well as the correlation of disturbed L-band signals transmitted by GNSS satellites on the same transionsopheric path. Our results confirm the effectiveness of the low-latitude scintillation simulation tools in generating real-world-like scintillation time series.

The results of processing both real and synthetic scintillation data confirm that GNSS signals are susceptible to ionospheric scintillation in regions where small-scale irregularities in electron density develop. In addition, lower frequency signals are affected more by scintillation when compared to higher frequency signals (this confirms equations (17) and (18) in *Van Dierendonck et al.* [1993]). Based on our results, deep signal fades ($\geq$15 dB) and large phase fluctuations ($\geq$0.2 cycles) are manifested, respectively, in large S_4 values ($\geq$0.5) and large σ_ϕ values ($\geq$0.25 radians).

As shown in Figures 8–11, at low S_4 values, the correlation coefficients between L1 and L2C signal intensities are dominated by receiver noise which is uncorrelated between the two signals. Otherwise, both the intensity and phase correlation between L1 and L2C decreases as the scintillation level increases. In particular, L1/L2CM decorrelation begins for intensity scintillation when $S_4 \geq 0.4$, and for phase scintillation when $\sigma_\varphi \geq 0.25$.

Finally, the impact of L1/L2C equatorial ionospheric scintillation on GNSS receivers (more specifically, the high-end GSNRx™ receiver) is investigated using real and simulated scintillation data. According to our results shown in Figures 13 and 14, the performance of the receiver under study is significantly high even under severe scintillation scenarios, with the highest probability of loss of phase lock equals to %0.68 on L1 and %2.31 on L2CM assuming the more conservative loss of

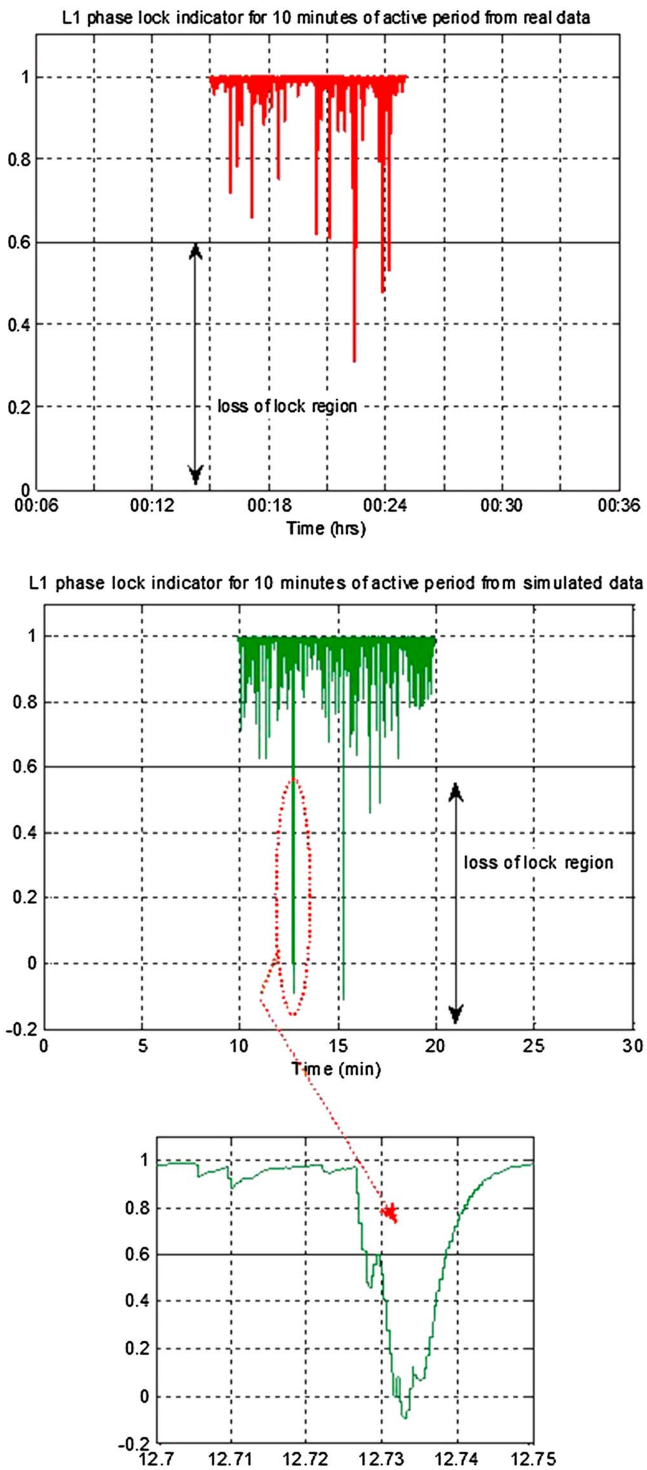

Figure 23. PLI with loss of phase lock for PLI < 0.6 for 10 min of active scintillation period from (top) real data and (middle) simulated signal. For clarification, the result of simulated signal is zoomed in between minutes 12 and 13 in Figure 23 (bottom).

phase lock threshold of PLI < 0.86 in the carrier tracking loops.

9. Future Studies

The impact of L-band equatorial ionospheric scintillation on a high-end GNSS receiver is explored in this work using real data on GPS L1/L2C signals and synthetic data on GPS L1 signal only. Modifying/extending the scintillation simulation algorithm to generate scintillation on multiple GNSS signals (e.g., GPS L1/L2C/L5), all propagating through the same transionospheric path, is the main focus of our current and future research. As shown for real data sets in this study, incorporating appropriate correlations between simulated multi-frequency GNSS signals is necessary and, therefore, should be considered in modified simulation algorithms. Moreover, by deploying our new data acquisition systems in high-latitude regions in near future, the impact of high-latitude ionospheric scintillation on GNSS receivers will be explored and required modifications to the scintillation simulation tool will be applied accordingly.

Appendix A

A1. Data Treatment

Data treatment (here the choice of detrending filter order and cutoff frequency) plays an important role in characterizing and determining scintillation indices; improper parameters may result in unrealistic large or small derived values. The implementation of non-causal and cascaded filters instead of the typically used causal filters is discussed in the section.

Non-causal Filters: Detrended signal intensity SI is required to determine the intensity scintillation index S_4. Detrended SI is obtained via normalizing SI to its low-pass filtered version. When operating in real time, the low-pass filter is implemented to be *causal*. The output of such filter depends only on present and past inputs. Causal filters, however, cannot be constructed such that its output has zero-phase shift with respect to the input signal. As a result, the low-frequency trend of SI might not completely be removed as we expect. To clarify this, about 250 s (from second 50 to 300) of the GPS PRN12 L1 signal intensity

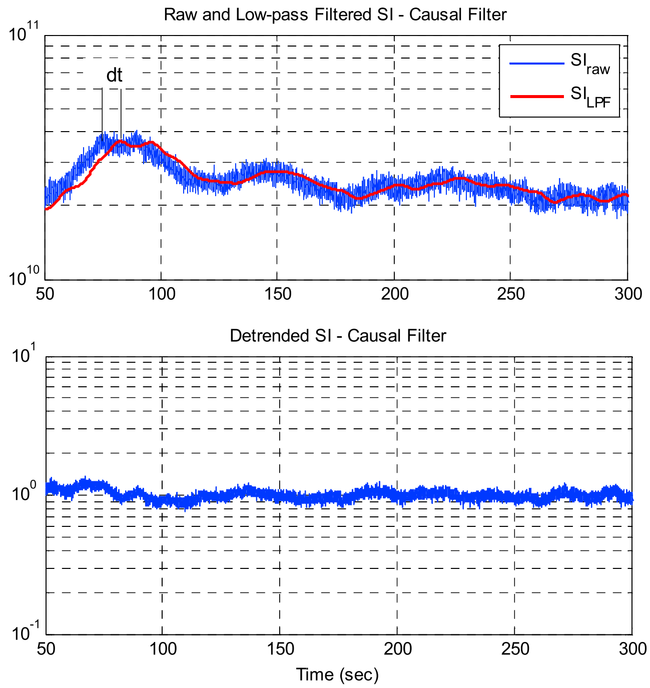

Figure A1. (top) Raw and low-pass filtered signal intensity using the sixth-order causal Butterworth filter with a 0.1 Hz cutoff frequency, and the (bottom) result of poorly detrended signal intensity. The signal intensities displayed in the plots are calculated from real data collected on GPS satellite PRN12 on 24 and 25 October (2012).

(including raw, low-pass filtered, and detrended SI) is shown in Figure A1. In this figure, $SI_{det}(t)$ at time t is calculated from $SI_{raw}(t)/SI_{LPF}(t)$ instead of $SI_{raw}(t)/SI_{LPF}(t-dt)$ with dt being the filter's time delay. Using the causal filter for the entire 4 h long data set, the corresponding S_4 indices are calculated and shown in Figure A2. As can be seen from this figure, unrealistically large S_4 indices (i.e., $S_4 > 1.5$) are usually the result of inappropriate data treatment rather than being indicators of severe intensity scintillation. This problem can be overcome via utilizing a *non-causal* filter. The output of a non-causal filter depends on the past, present, and future inputs, and has a zero-phase shift with respect to the input signal. This filter can easily be implemented in post-processing mode. The transfer function of a non-causal filter, $H_{nc}(z)$, is related to that of a causal filter, $H_c(z)$, via [*Mouffak and Belbachir*, 2012]

$$H_{nc}(z) = H_c(z) \cdot H_c(1/z) \quad \text{(A1)}$$

Based on equation (A1), a non-causal filter is implemented using a combination of causal filtering and time reversal. As shown in Figure A3, first, a stable recursive digital filter is applied to the input sequence $x[n]$. Following that, a non-causal subsystem is implemented via a time reversal operation, a recursive digital filter, and another time reversal operation. This process is illustrated in Figure A3 considering $x[n]$ and $y[n]$ as the input and output sequences. As comparison to Figure A1, the results of applying a non-causal filter in detrending signal intensity is shown below in Figure A4. Zero-phase shift between SI_{raw} and SI_{LPF} is obvious in the figure, and no low-frequency trend is observed in the resulting SI_{det}. The subsequent intensity scintillation index is shown earlier in Figure 3.

Cascaded Filters: Utilizing a non-causal filter in post-processing mode can solve the problem of filter delays as discussed above. In real-time processing, however, no information about future data samples is available; as a result, a non-causal filter cannot be implemented. To overcome the problem of phase shift between the filter's input and output, a cascade of lower order causal filters can be employed instead. In this work, a cascade of six first-order high-pass Butterworth filters with a 0.035 Hz cutoff frequency is used as a better alternative for the typically used sixth-order high-pass Butterworth filter with a 0.1 Hz cutoff frequency. The cutoff frequency of each lower order filter is given below.

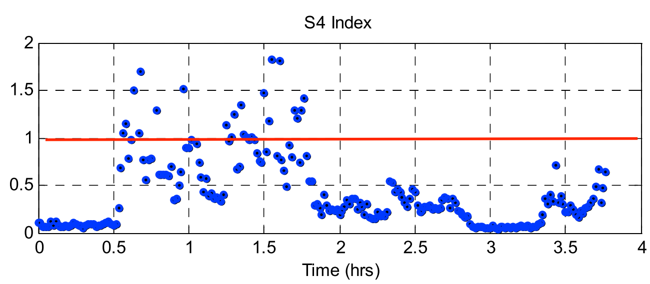

Figure A2. Intensity scintillation index S_4 calculated for the entire 4 h long data session (collected on GPS satellite PRN12 on 25 October 2012) using causal filter in signal detrending.

First-order high-pass and low-pass filters have transfer functions of the form

$$H_{HP}(s) = \frac{ks}{s + w_c} \quad \text{(A2)}$$

$$H_{LP}(s) = \frac{kw_c}{s + w_c} \quad \text{(A3)}$$

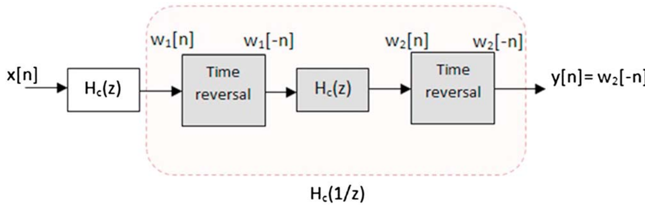

Figure A3. Non-causal recursive digital filter structure.

with w_c being the corner frequency and k being the low-frequency (DC) gain (here DC gain refers to the value of transfer function at 0 Hz or $s = 0$). In each case, the term *cutoff frequency* w_{cutoff} refers to the frequency at which

$$|H(jw_{cutoff})| = \frac{1}{\sqrt{2}} \max|H(jw)| \tag{A4}$$

To find the cutoff frequency for a first-order low-pass filter, one needs to solve

$$\frac{kw_c}{\sqrt{w^2 + w_c^2}} = \frac{k}{\sqrt{2}} \tag{A5}$$

which gives that the cutoff frequency equals the corner frequency $w = w_c$. Similarly, to find the cutoff frequency for a first-order high-pass filter, one needs to solve

$$\frac{kw}{\sqrt{w^2 + w_c^2}} = \frac{k}{\sqrt{2}} \tag{A6}$$

which again results in $w = w_c$.

When N first-order low-pass filters are cascaded to form an Nth-order low-pass filter with $w = w'_{cutoff}$ cutoff frequency, the cutoff frequency of each inner filter is calculated from

$$\frac{w_c}{\sqrt{w^2 + w_c^2}} = \left(\frac{1}{\sqrt{2}}\right)^{1/N} \tag{A7}$$

Solving for w will result in

$$w = w'_{cutoff} = w_c\sqrt{2^{1/N} - 1} \tag{A8}$$

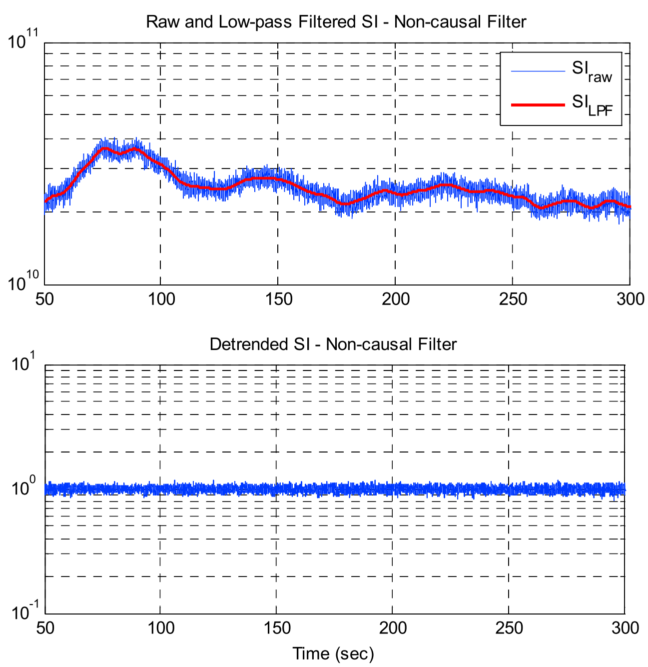

Figure A4. (top) Raw and low-pass filtered signal intensity using the sixth-order non-causal Butterworth filter with a 0.1 Hz cutoff frequency and (bottom) detrended signal intensity.

As an example, for having a sixth-order low-pass Butterworth filter with $w'_{cutoff} = 0.1$ Hz, the cutoff frequency of each first-order low-pass filter would be $w_c = 0.2858$ Hz. Similarly, the cutoff frequency of N cascade first-order high-pass filter can be calculated from

$$\frac{w}{\sqrt{w^2 + w_c^2}} = \left(\frac{1}{\sqrt{2}}\right)^{1/N} \tag{A9}$$

Solving for w will result in

$$w = w'_{cutoff} = \frac{w_c}{\sqrt{2^{1/N} - 1}} \tag{A10}$$

For having a sixth-order high-pass Butterworth filter with $w'_{cutoff} = 0.1$ Hz cutoff frequency, the cutoff frequency of each first-order high-pass filter would be $w_c = 0.035$ Hz. Note that even though first-order filters are considered here as building blocks of a cascaded higher-order filter, the inner filters do not have to be of the same order.

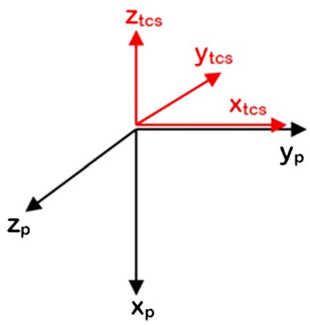

Figure A5. Receiver coordinates in TCS system versus propagation system.

A2. Propagation Parameters

The calculation of the propagation parameters in the propagation coordinate system employed in Rino's model [*Rino*, 2011] is given below.

Satellite range and range rate: if $\mathbf{x}_{sat,tcs}(t) = [x_1(t), x_2(t), x_3(t)]$ and $\mathbf{v}_{sat,tcs}(t) = [v_1(t), v_2(t), v_3(t)]$ represent the satellite position and velocity vectors in the receiver Topocentric Coordinate System (TCS), respectively, with the system's origin being at the receiver location, then the satellite range (in meter) and range rate (in m/s) can be calculated via

$$\mathrm{sat}_{range}(t) = \sqrt{x_1^2(t) + x_2^2(t) + x_3^2(t)} \tag{A11}$$

$$\begin{aligned}\mathrm{sat}_{rangerate}(t) &= \mathbf{v}_{sat,tcs}(t) \cdot \mathbf{u}_{sat,tcs}(t) \\ &= v_1(t)u_1(t) + v_2(t)u_2(t) + v_3(t)u_3(t)\end{aligned} \tag{A12}$$

where the unit vector $\mathbf{u}_{sat,tcs}$(t) is defined as

$$\mathbf{u}_{sat,tcs}(\mathrm{t}) = [\mathrm{u}_1(\mathrm{t}), \mathrm{u}_2(\mathrm{t}), \mathrm{u}_3(\mathrm{t})] = \mathbf{x}_{sat,tcs}(\mathrm{t})/\mathrm{sat}_{range}(\mathrm{t}) \tag{A13}$$

Satellite elevation and azimuth angles: using $\mathbf{x}_{sat,tcs}(t)$, the elevation and azimuth angles (in degrees) are obtained from

$$\mathrm{sat}_{elevation}(t) = \mathrm{atan}\left(\frac{x_3(t)}{\sqrt{x_1^2(t) + x_2^2(t)}}\right) \tag{A14}$$

$$\mathrm{sat}_{azimuth}(t) = \mathrm{atan}\left(\frac{x_2(t)}{x_1(t)}\right) \tag{A15}$$

IPP position and range to the ground station: Ionospheric Pierce Point (IPP) or the satellite signal penetration point is the intersection point between the satellite-receiver line of sight and the ionosphere shell (nominally taken as 350 km). IPP location $\mathbf{x}_{IPP}(t) = [\phi_{IPP}, \lambda_{IPP}, h_{IPP}]$, can be computed in the geodetic coordinate system via

$$\begin{aligned}\phi_{IPP}(t) &= \varphi_r(t) + \psi \cos\left(\mathrm{sat}_{azimuth}(t)\right) \\ \lambda_{IPP}(t) &= \lambda_r(t) + \psi \frac{\sin\left(\mathrm{sat}_{azimuth}(t)\right)}{\cos(\varphi_{IPP}(t))} \\ h_{IPP}(t) &= h\end{aligned} \tag{A16}$$

in which

$$\psi = \cos^{-1}\left(\left(\frac{R_E}{R_E + h}\right)\cos(\mathrm{sat}_{elev}(t))\right) - \mathrm{sat}_{elev}(t) \tag{A17}$$

where h represents the phase screen height ($h = 350$ km), R_E represents the mean radius of the spherical Earth ($R_E = 6371$km) and (ϕ_r, λ_r) represent the receiver latitude and longitude. The scintillation wavefield is initiated at phase screen height and then propagated toward the ground station. The calculation of the propagation reference coordinate system (x_p, y_p, z_p) for the IPP point to the receiving antenna is done in two steps. First, the coordinates of the receiver $\mathrm{rec}_{llh}(t) = [\phi_r(t), \lambda_r(t), h_r(t)]$ are calculated in a TCS system centered on the IPP point. Here the subscript llh refers to latitude, longitude, and height, respectively. With these TCS coordinates $(x_{tcs}, y_{tcs}, z_{tcs})$, the propagation system coordinates (x_p, y_p, z_p), as shown in Figure A5, are obtained via

$$\begin{aligned}x_p(t) &= -z_{tcs}(t) \\ y_p(t) &= +x_{tcs}(t) \\ z_p(t) &= -y_{tcs}(t)\end{aligned} \tag{A18}$$

From this equation, the IPP range (in meter) to the ground station is derived as

$$\mathrm{IPP}_{\mathrm{range}}(t) = \sqrt{x_{\mathrm{p}}^2(t) + y_{\mathrm{p}}^2(t) + z_{\mathrm{p}}^2(t)} \tag{A19}$$

Propagation angles: using equation (A18), the propagation angles (in degrees) can be calculated via

$$\theta_{\mathrm{p}}(t) = \tan^{-1}\left(\sqrt{y_{\mathrm{p}}^2(t) + z_{\mathrm{p}}^2(t)}/x_{\mathrm{p}}(t)\right) \tag{A20}$$

$$\varphi_{\mathrm{p}}(t) = \tan^{-1}\left(z_{\mathrm{p}}(t)/y_{\mathrm{p}}(t)\right) \tag{A21}$$

Signal penetration point velocity: from $\mathbf{v}_{\mathrm{sat,tcs}}(t) = [v_1(t), v_2(t), v_3(t)]$, the penetration point velocity (in m/s) components can be achieved via

$$\begin{aligned} v_{\mathrm{px}}(t) &= -v_3(t)\cdot v_{\mathrm{SF}} \\ v_{\mathrm{py}}(t) &= +v_1(t)\cdot v_{\mathrm{SF}} \\ v_{\mathrm{pz}}(t) &= -v_2(t)\cdot v_{\mathrm{SF}} \end{aligned} \tag{A22}$$

where the scale factor is defined as

$$v_{\mathrm{SF}} = \frac{\mathrm{IPP}_{\mathrm{range}}(t)}{\mathrm{sat}_{\mathrm{range}}(t)} \tag{A23}$$

Apparent velocities in the measurement plane: the apparent velocity in the measurement plane is obtained via

$$\begin{aligned} v_{k_{\mathrm{east}}}(t) &= -v_{\mathrm{py}}(t) + \tan(\theta_{\mathrm{p}}(t))\cdot\cos\left(\varphi_{\mathrm{p}}(t)\right)\cdot v_{\mathrm{px}}(t) \\ v_{k_{\mathrm{south}}}(t) &= -v_{\mathrm{pz}}(t) + \tan(\theta_{\mathrm{p}}(t))\cdot\sin\left(\varphi_{\mathrm{p}}(t)\right)\cdot v_{\mathrm{px}}(t) \end{aligned} \tag{A24}$$

Acknowledgments
The IF data used in this research has been collected under a cooperation project between the Brazilian Institute of Geography and Statistics (IBGE), the University of the State of Rio de Janeiro (UERJ), Brazil, and the Position, Location and Navigation (PLAN) Group of the Department of Geomatics Engineering, University of Calgary, Canada, with Luiz Paulo Souto Fortes, PhD (IBGE, UERJ) and Gérard Lachapelle (PLAN Group) as principal investigators.

References

Afraimovich, E. L., V. V. Demyanov, P. V. Tatarinov, E. I. Astafieva, and I. V. Zhivetiev (2006), GPS users positioning errors during disturbed near-Earth space conditions, *Characterizing the Ionosphere*, Meeting Proceedings RTO-MP-IST-056, pp. 1–14.
Alfonsi, L., L. Spogli, J. R. Tong, G. De Franceschi, V. Romano, A. Bourdillon, M. Le Huy, and C. N. Mitchell (2010), GPS scintillation and TEC gradients at equatorial latitudes in April 2006, *Adv. Space Res.*, *47*(10), 1750–1757.
Carrano, C. S., and K. M. Groves (2010), Temporal decorrelation of GPS satellite signals due to multiple scattering from ionospheric irregularities, in *Proceedings of the 23rd International Technical Meeting of The Satellite Division of the Institute of Navigation* (*ION GNSS 2010*), pp. 361–374, Portland, Oreg.
Carrano, C. S., K. M. Groves, W. J. McNeil, and P. H. Doherty (2012), Scintillation characteristics across the GPS frequency band, in *Proceedings of the 25th International Technical Meeting of The Satellite Division of the Institute of Navigation* (*ION GNSS 2012*), pp. 1972–1989, Nashville, Tenn.
Conker, R. S., M. B. El-Arini, C. J. Hegarty, and T. Hsiao (2003), Modeling the effects of ionospheric scintillation on GPS/Satellite-based augmentation system availability, *Radio Sci.*, *38*(1), 1001, doi:10.1029/2000RS002604.
De Rezende, L. F. C., E. R. de Paula, I. S. Batista, I. J. Kantor, and M. T. de Assis Honorato Muella (2007), Study of ionospheric irregularities during intense magnetic storms, *Rev. Bras. Geofis.*, *25*(supl. 2), 151–158.
Finlay, C. C., et al. (2010), International geomagnetic reference field: The eleventh generation, *Geophys. J. Int.*, *183*(3), 1216–1230.
Fremouw, E. J., R. L. Leadabrand, R. C. Livingston, M. D. Cousins, C. L. Rino, B. C. Fair, and R. A. Long (1978), Early results from the DNA wideband satellite experiment—Complex-signal scintillation, *Radio Sci.*, *13*(1), 167–187, doi:10.1029/RS013i001p00167.
Jwo, D. J. (2001), Optimisation and sensitivity analysis of GPS receiver tracking loops in dynamic environments, *IEE Proc., Radar-Sonar Navig.*, *148*(4), 241–250.
Klobuchar, J. A. (1996), Ionospheric effects on GPS, in *Global Positioning System: Theory and Application*, vol. 1, edited by B. W. Parkinson and J. J. Spilker, chap. 12, pp. 485–515, Am. Inst. of Aeronaut. and Astronaut., Washington, D. C.
Knight, M. F., and A. Finn (1998), The effects of ionospheric scintillations on GPS, paper presented at 11th International Technical Meeting of the Satellite Division of The Institute of Navigation (ION GPS 1998), pp. 673–685, Nashville, Tenn.
Mongredien, C., G. Lachapelle, and M. E. Cannon (2006), Testing GPS L5 acquisition and tracking algorithms using a hardware simulator, in *Proceedings of ION GNSS 2006*, pp. 2901–2913, Institute of Navigation, Fort Worth, Tex.
Mouffak, A., and M. F. Belbachir (2012), Noncausal forward/backward two-pass IIR digital filters in real time, *Turk. J. Electr. Eng. Comput. Sci.*, *20*(5), 769–786.
O'Driscoll, C., D. Borio, M. Petovello, T. Williams, and G. Lachapelle (2009), The soft approach: A recipe for a multi-system, multi-frequency GNSS receiver, *Inside GNSS*, *4*, 46–51.
Rino, C. L. (1979), A power law phase screen model for ionospheric scintillation. 1. Weak scatter, *Radio Sci.*, *14*(6), 1135–1145, doi:10.1029/RS014i006p01135.
Rino, C. L. (1982), On the application of phase screen models to the interpretation of ionospheric scintillation data, *Radio Sci.*, *17*(4), 855–867, doi:10.1029/RS017i004p00855.

Rino, C. L. (2011), *The Theory of Scintillation With Applications in Remote Sensing*, Wiley-IEEE Press, Hoboken, N. J.

Spirent (2008), SimGEN User Manual, software for the spirent range of satellite navigation simulator products, published as Rep. 1–28.

Van Dierendonck, A. J. (1996), GPS receivers, in *Global Positioning System: Theory and Application*, vol. 1, edited by B. W. Parkinson and J. J. Spilker, chap. 8, pp. 329-407, Am. Inst. of Aeronaut. and Astronaut., Washington, D. C.

Van Dierendonck, A. J., J. Klobuchar, and Q. Hua (1993), Ionospheric scintillation monitoring using commercial single frequency C/A code receivers, in *Proceedings of the 6th International Technical Meeting of the Satellite Division of The Institute of Navigation* (*ION GPS 1993*), pp. 1333–1342, Salt Lake City, UT.

Wernik, A. W., J. A. Secan, and E. J. Fremouw (2003), Ionospheric irregularities and scintillation, *Adv. Space Res.*, *31*(4), 971–981.

Zhang, L., Y. Morton, F. van Graas, and T. Beach (2010), Characterization of GNSS signal parameters under ionosphere scintillation conditions using software-based tracking algorithms, in *Proceedings of IEEE/ION PLANS 2010*, pp. 264–275, Indian Wells, Calif.